Journal Pre-proofs


# Peridynamic analysis of materials interface fracture with thermal effect

Heng Zhang, Xiong Zhang

PII: S0167-8442(22)00168-9
DOI: https://doi.org/10.1016/j.tafmec.2022.103420
Reference: TAFMEC 103420

To appear in: *Theoretical and Applied Fracture Mechanics*

Received Date: 25 February 2022
Revised Date: 16 May 2022
Accepted Date: 24 May 2022

Please cite this article as: H. Zhang, X. Zhang, Peridynamic analysis of materials interface fracture with thermal effect, *Theoretical and Applied Fracture Mechanics* (2022), doi: https://doi.org/10.1016/j.tafmec.2022.103420

# Peridynamic analysis of materials interface fracture with thermal effect[1]

**Heng Zhang[*], Xiong Zhang[**]**

[a] *School of Aerospace Engineering, Tsinghua University, Beijing 100084, China*

**Abstract:** A thermomechanical peridynamic framework is established for fracture analysis of dissimilar material interface coupled with residual thermal effect. In this frame, an extended peridynamic mixed-mode failure model considering thermal effect is proposed for interfacial fracture prediction, and the peridynamics-based methods for interface crack energy release rate and mode mixity computations are given. Meanwhile, a new peridynamic contact model is proposed for frictional contact modeling of crack surfaces. Then, three examples of the single edge-notched bimaterial (SENB), asymmetric bimaterial cantilever beams (ABCB) and four-point shearing (FPS) tests, are analyzed for the model verification and application. The elastic and interfacial fracture behaviors of these tests are predicted by the proposed peridynamic models, and compared to the analytical and the FEM solutions. The results show that the proposed peridynamic models can successfully predict the failure characteristics of materials interface, and capture the role of residual thermal effect on the interfacial fracture.

Keywords: peridynamics; residual thermal effect; interfacial fracture; frictional contact.

## 1. Introduction

Consolidation of bonded or layered structures are commonly achieved by co-firing operation at high temperature. During cool-down, residual thermal deformations are generated in these structures due to the mismatch of materials thermal expansion coefficients, which would lead to stress concentration in material interfaces, and greatly affect the fracture characteristics of interface cracks. Therefore, the investigation of fracture properties of material interface with residual thermal deformation is essential for the reliability and performance predictions of layered systems.

[*] Email: hengzh@tsinghua.edu.cn

[**] Corresponding author. Email: xzhang@tsinghua.edu.cn

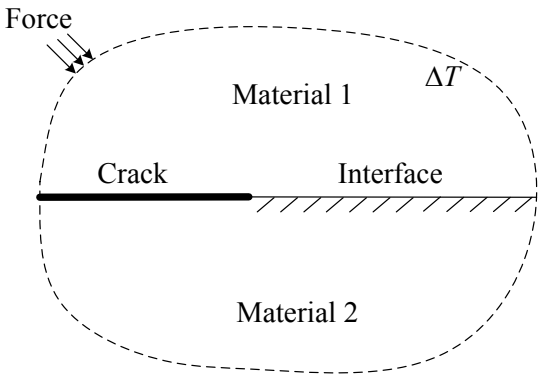


**Fig. 1.** An interface crack in bonded dissimilar materials with the residual thermal and mechanical loads.

Based on fracture mechanics, an interface crack contained in bonded dissimilar materials has been theoretically analyzed as shown in Fig. 1, in which the residual thermal and mechanical loads are simultaneously considered. The stress intensity factor and energy release rate of the interface crack were defined and computed [1,2], and the effect of residual stresses on bimaterial interface delamination was investigated [3,4]. However, the analytical solutions are only available for a few special cases. The experimental study was of great importance and necessity to investigate the interface fracture toughness with the thermal effect [5,6], but the interface fracture experiment costs too much since it is always one-time failure test. The numerical method, like the Finite Element Method (FEM), has a great advantage for deformation analysis of bimaterial structures with thermal residual stresses [7]. And it also has been applied to investigate fracture behaviors of material interfaces, incorporated with the virtual crack extension (VCE) [8,9] and virtual crack closure technique (VCCT) methods [10]. However, the original FEM method is based on classical local theory with displacement continuity assumption, remeshing is required when the crack path is unknown, and the complex fracture criteria are needed [11]. Recently, other numerical methods, like generalized finite difference method [12] and extended finite element method [13], were also utilized for the fracture mechanics analysis of bimaterial interface. And the progresses of interface crack initiation and propagation due to the thermomechanical loads were investigated by the finite fracture mechanics [14], cohesive zone model [15] and nonlocal continuum theory [16]. However, it is still great challenge to fully predict the thermal effects on interface fracture behaviors, i.e., interface crack initiation, kinking nucleation and crack path selection.

Peridynamics (PD) [17] was proposed as a nonlocal reformulation of classical solid

mechanics, in which the continuous body is divided into finite material points, and the points interact with each other within a certain horizon. In peridynamic theory, the integral-differential equations are used to replace the partial differential equations. Thus, the inadequacies of continuous mechanics on discontinuous problems are removed, and peridynamics can be naturally utilized for fracture problems, such as crack modeling and interfacial fracture. Generally, there are three types of peridynamic models called as, bond-based peridynamics (BB-PD) [17], ordinary state-based peridynamics (OSB-PD) [18,19] and non-ordinary state-based peridynamics (NOSB-PD) [20,21]. As the original version of peridynamics, the BB-PD model was firstly proposed in 2000. In BB-PD, the peridynamic material points are connected with spring-like interactions, which leads to the value restrictions of Poisson's ratio. To remove these restrictions, the state-based peridynamics (SB-PD) [18] was then proposed as a more general frame, in which material points interact with each other via all deformations of their horizons. Furthermore, in the OSB-PD model, the deformation state of material response can be explicitly employed as the volumetric and distortional parts, and the materials in continuous mechanics can be reproduced [18,22–26]. While in the NOSB-PD model, the bond force state is not required parallel to deformed position of connected bond, and the peridynamic beam, plates and flat shells have been modeled [27–30].

For quantitatively analysis of fracture problems, various peridynamic failure models for bond failure predictions have been successively proposed, such as the critical stretch [31,32], critical bond energy density [33] and critical skew angle models [34]. Recently, a mixed-mode bond failure model was proposed for fracture analysis of mixed-mode interface cracks [35]. The coupled strength and fracture failure models were proposed for the problems with non-singular stress raisers [36–38]. Meanwhile, the essential fracture parameter, energy release rate (ERR), has been computed in peridynamic theory by the reformulated methods of the J-integral [39,40], crack extension technique [41], and virtual crack closure technique [42]. The fracture methods, like cohesive zone model [43–45] and phase field theory [46] were also coupled with peridynamics for failure analysis.

With the nature capability on discontinuity modeling, peridynamics has been applied for failure analysis of various problems [47–54]. And the thermal coupled problems were also investigated. The peridynamic elastic models considering thermal expansion effect were

proposed for the thermomechanical analysis [55–59]. Transient heat conduction problems were analyzed by peridynamics with evolving discontinuities [60–62]. Fully coupled peridynamic thermomechanics were then established by using thermodynamics [63,64], which was further extended for fully coupled thermomechanical analysis of laminated composite [65], concrete [66] and granite [67]. Meanwhile, peridynamics has also been applied for the fracture analysis of material interfaces. The peridynamic elastic interface models were introduced with the convergence study to the classical local interface theory [68,69]. Recently, the authors [70] proposed a general peridynamics-based framework for elastic bimaterial interface fracture analysis. However, in above studies, the role of residual thermal effect on interface fracture has not been well investigated, which is essential for the fracture behavior predictions of materials interface.

Generally, for the interface fracture problems with thermal effects, there are three main issues need to be carefully considered. First, the mismatches of thermal expansion coefficients and mechanical properties would lead to residual thermo-mechanical deformations and stress concentrations around the interface. Meanwhile, with the coupled loads, the interface cracks are mostly in the mixed-mode conditions, and the crack mode mixity is strongly influenced by the temperature variation. Last, the crack surfaces are commonly in contact when compressive stresses occur along the fracture surface because of residual thermal effects. Based on above issues, the following works in peridynamic theory need to be addressed for this topic:

- A peridynamic thermomechanical elastic model for residual thermo-mechanical deformation prediction;
- A mixed-mode peridynamic bond failure criterion for interface crack fracture modeling with thermal considering;
- Peridynamic methods for the energy release rate and mode mixity computations of interface cracks with thermal considering;
- A peridynamic contact model for frictional contact modeling of crack surfaces.

In this paper, a whole peridynamic-based frame is established for the fracture analysis of dissimilar material interface with the residual thermal effect. First, the peridynamic thermomechanical elastic model is presented, and the forms of bond force scaler and bond energy density considering thermal effect are given. An extended peridynamic mixed-mode

bond failure criterion is introduced for interface bond failure prediction, and the peridynamic methods for energy release rate and mode mixity computations are given. The peridynamic contact model is also proposed for frictional contact modeling of crack surfaces. Then, three examples of the single edge-notched bimaterial (SENB), asymmetric bimaterial cantilever beams (ABCB) and four-point shearing (FPS) tests, are analyzed for the model verification and application. The elastic and fracture behaviors of these tests are predicted by the proposed peridynamic models, and compared to the analytical and the FEM solutions.

## 2. Peridynamic thermomechanical model

In peridynamic theory, a continuous body is separated into finite material points, and the material points interact with each other within their horizons by peridynamic "bonds". The equation of motion for a material point $\mathbf{x}$ takes the form of [18]:

$$\rho(\mathbf{x})\ddot{\mathbf{u}}(\mathbf{x},t)=\int_{H_x}\left\{\underline{\mathbf{T}}[\mathbf{x},t]\langle\mathbf{x}'-\mathbf{x}\rangle-\underline{\mathbf{T}}[\mathbf{x}',t]\langle\mathbf{x}-\mathbf{x}'\rangle\right\}\mathrm{d}V_{\mathbf{x}'}+\mathbf{b}(\mathbf{x},t) \tag{2}$$

where $\rho$ is the density of point $\mathbf{x}$, $\mathbf{u}$ is the displacement at time $t$, $\mathbf{x}'$ is the neighbor point of point $\mathbf{x}$ in its neighborhood $H_x$, where the cut-off radius $\delta$ is considered as nonlocal horizon (see Fig. 2), and $\mathbf{b}(\mathbf{x},t)$ is the body force density. As shown in Fig. 2, $\boldsymbol{\xi}=\mathbf{x}'-\mathbf{x}$ is the bond vector, $\underline{\mathbf{X}}\langle\boldsymbol{\xi}\rangle$ and $\underline{\mathbf{Y}}\langle\boldsymbol{\xi}\rangle$ are its reference and deformed vectors, and $\underline{\mathbf{T}}[\mathbf{x},t]$ and $\underline{\mathbf{T}}[\mathbf{x}',t]$ are the force vector states of points $\mathbf{x}$ and $\mathbf{x}'$, respectively. In the ordinary state-based peridynamic theory, the force vector of bond $\boldsymbol{\xi}$ can be expressed as [18]:

$$\underline{\mathbf{T}}[\mathbf{x},t]\langle\boldsymbol{\xi}\rangle=\underline{t}\langle\boldsymbol{\xi}\rangle\frac{\underline{\mathbf{Y}}\langle\boldsymbol{\xi}\rangle}{|\underline{\mathbf{Y}}\langle\boldsymbol{\xi}\rangle|} \tag{3}$$

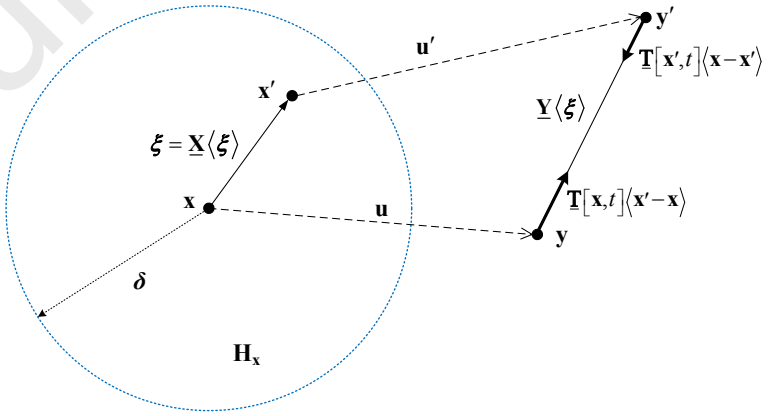


**Fig. 2.** Ordinary state-based peridynamic model.

where $\underline{t}$ is the force scalar state that reflects the relationship of the deformation and force states,

and its formation can be deduced by energy density equivalence between peridynamic and classical mechanic theories.

### 2.1. Peridynamic elastic model with thermomechanical effect

In the ordinary state-based model, the peridynamic strain energy density $W_{\mathrm{PD}}$ considering the thermomechanical effect can be expressed as [57]:

$$W_{\mathrm{PD}} = \frac{\kappa\theta^2}{2} + \frac{\alpha}{2}\left(\underline{\omega e}\right)\bullet\underline{e} - 3\beta'\theta\Delta T + f\left(\Delta T\right) \tag{4}$$

where $\kappa$, $\alpha$ and $\beta'$ are the peridynamic constants, $\theta$ is the nonlocal dilatation that is defined for three dimensional and plane problems as:

$$\theta = \begin{cases} 3\dfrac{\underline{\underline{\omega x}}\bullet\underline{e}}{q}; & \text{3D} \\ 2\dfrac{\underline{\underline{\omega x}}\bullet\underline{e}}{q}; & \text{2D} \end{cases} \tag{5}$$

where $\underline{\omega}$ is the influence function, $\underline{x}$ is equal to the bond length state $\left|\underline{\mathbf{X}}\right|$, $\underline{e}$ is the extension scalar state, $q$ is the weighted volume defined by $q = \left(\underline{\omega x}\right)\bullet\underline{x}$, $\left(\bullet\right)$ is the dot product of two states as $\underline{\mathbf{A}}\bullet\underline{\mathbf{B}} = \int_{\mathrm{H_x}}\left(\underline{\mathbf{AB}}\right)\langle\boldsymbol{\xi}\rangle\mathrm{d}V_{\boldsymbol{\xi}}$, and $\Delta T$ is the temperature variation. Thus, the first two terms of the strain energy density are related to mechanical deformation state, $f\left(\Delta T\right)$ is the strain energy density due to temperature change, while the third part is related to the coupled effect of mechanical and thermal states. Considering energy density equivalence to continuous mechanics, the peridynamic constants and $f\left(\Delta T\right)$ in Eq. (4) take the forms of:

$$\begin{cases} \kappa = k' - \dfrac{5}{3}\mu,\ \alpha = \dfrac{15\mu}{q},\ \beta' = k'\beta,\ f\left(\Delta T\right) = \dfrac{9}{2}k'\beta^2(\Delta T)^2 & \text{3D} \\ \kappa = k' - 2\mu,\ \alpha = \dfrac{8\mu}{q},\ \beta' = \dfrac{2}{3}k'\beta,\ f\left(\Delta T\right) = 2k'\beta^2(\Delta T)^2 & \text{Plane Stress} \\ \kappa = k' - 2\mu,\ \alpha = \dfrac{8\mu}{q},\ \beta' = \dfrac{2\left(1+\nu\right)}{3}k'\beta,\ f\left(\Delta T\right) = 3\left(1+\nu\right)k'\beta^2(\Delta T)^2 & \text{Plane Strain} \end{cases} \tag{6}$$

where $\mu$ is the shear modulus, $\beta$ is the coefficient of thermal expansion, $k'$ is the bulk modulus that can be expressed in terms of the Young's modulus $E$ and the Poisson's ratio $\nu$ as:

$$k'=\begin{cases}\dfrac{E}{3(1-2v)} & \text{3D}\\ \dfrac{E}{2(1-v)} & \text{Plane stress}\\ \dfrac{E}{2(1+v)(1-2v)} & \text{Plane strain}\end{cases} \tag{7}$$

The peridynamic force scalar state $\underline{t}$ in Eq. (2) can be obtained by taking the Frechet derivative of the strain energy density $W_{\mathrm{PD}}$, as $\underline{t}=\nabla_{\underline{e}}W_{\mathrm{PD}}$. Thus, the form of force scalar state with the thermomechanical effect is obtained as:

$$\underline{t_T}=\begin{cases}3\dfrac{\underline{\underline{\omega x}}}{q}\left(\left(k'-\dfrac{5}{3}\mu\right)\theta-3k'\beta\Delta T\right)+\dfrac{15\mu}{q}\underline{\omega e} & \text{3D}\\ 2\dfrac{\underline{\underline{\omega x}}}{q}\left(\left(k'-2\mu\right)\theta-2k'\beta\Delta T\right)+\dfrac{8\mu}{q}\underline{\omega e} & \text{Plane Stress}\\ 2\dfrac{\underline{\underline{\omega x}}}{q}\left(\left(k'-2\mu\right)\theta-2\left(1+v\right)k'\beta\Delta T\right)+\dfrac{8\mu}{q}\underline{\omega e} & \text{Plane Strain}\end{cases} \tag{8}$$

where the italics subscript $T$ is used for distinguishing of thermal considering. While when the temperature variation is not considered, the force scalar state can be reduced as:

$$\underline{t}=\begin{cases}3\dfrac{\underline{\underline{\omega x}}}{q}\left(k'-\dfrac{5}{3}\mu\right)\theta+\dfrac{15\mu}{q}\underline{\omega e} & \text{3D}\\ 2\dfrac{\underline{\underline{\omega x}}}{q}\left(k'-2\mu\right)\theta+\dfrac{8\mu}{q}\underline{\omega e} & \text{Plane Stress}\\ 2\dfrac{\underline{\underline{\omega x}}}{q}\left(k'-2\mu\right)\theta+\dfrac{8\mu}{q}\underline{\omega e} & \text{Plane Strain}\end{cases} \tag{9}$$

**2.2. Peridynamic bond energy density**

The energy density stored in the bond $\boldsymbol{\xi}$ was defined as the bond energy density $\underline{w}\langle\boldsymbol{\xi}\rangle$, which can be computed by the work done of the bond force density $\underline{\mathbf{T}}[\mathbf{x},t]\langle\boldsymbol{\xi}\rangle-\underline{\mathbf{T}}[\mathbf{x}',t]\langle-\boldsymbol{\xi}\rangle$ under its deformation scalar $\underline{\mathbf{Y}}\langle\boldsymbol{\xi}\rangle$ as:

$$\underline{w}\langle\boldsymbol{\xi}\rangle=\int_{\underline{\mathbf{X}}\langle\boldsymbol{\xi}\rangle}^{\underline{\mathbf{Y}}\langle\boldsymbol{\xi}\rangle}\left\{\underline{\mathbf{T}}[\mathbf{x},t]\langle\boldsymbol{\xi}\rangle-\underline{\mathbf{T}}[\mathbf{x}',t]\langle-\boldsymbol{\xi}\rangle\right\}\cdot\mathrm{d}\underline{\mathbf{Y}}\langle\boldsymbol{\xi}\rangle \tag{10}$$

In the ordinary state-based peridynamics, considering the linear elastic property and the temperature variation, the bond energy density with the thermal effect takes the form of:

$$\underline{w_T}\langle\boldsymbol{\xi}\rangle=\frac{1}{2}\left(\underline{t_T}\langle\boldsymbol{\xi}\rangle+\underline{t'_T}\langle\boldsymbol{\xi}\rangle\right)\cdot\underline{e_T}\langle\boldsymbol{\xi}\rangle \tag{11}$$

where $\underline{t_T}\langle\boldsymbol{\xi}\rangle$ and $\underline{t'_T}\langle\boldsymbol{\xi}\rangle$ are the force scalar of points **x** and $\mathbf{x}'$ that can be computed by Eq. (8). $\underline{e_T}\langle\boldsymbol{\xi}\rangle$ is the extension scalar of bond $\boldsymbol{\xi}$ with the thermomechanical effect, and it can be specifically expressed as:

$$\underline{e_T} = \begin{cases} \underline{e} - \beta\Delta T\,\underline{x} & \text{3D} \\ \underline{e} - \beta\Delta T\,\underline{x} & \text{Plane Stress} \\ \underline{e} - (1+\nu)\beta\Delta T\,\underline{x} & \text{Plane Strain} \end{cases} \tag{12}$$

### 2.3. Peridynamic interface model

In the material interface zone, as shown in Fig. 3, two dissimilar materials are connected by an interface with zero thickness, and the temperature variation is considered in interface zone. For this material interface modeling, the peridynamic interface bond is defined as the connection of different material points across the interface. For example, points **x1** and **x2**, which respectively belong to material 1 and material 2, are connected with the peridynamic interface bond vector $\boldsymbol{\xi}_{\mathbf{M}} = \mathbf{x2} - \mathbf{x1}$. In which $\mathrm{H}_{\mathbf{x1}}$ are $\mathrm{H}_{\mathbf{x2}}$ are their neighborhood horizons with the same cut-off radius $\delta$.

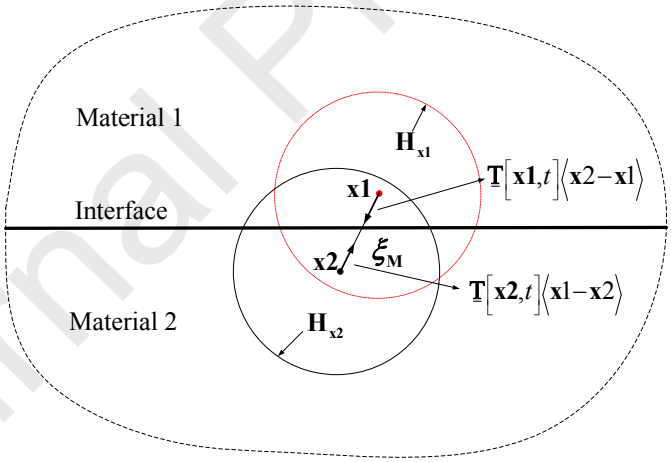


**Fig. 3.** Peridynamic interface model: points **x1** and **x2** in different material zones are connected by peridynamic interface bond $\boldsymbol{\xi}_{\mathbf{M}}$ with their typical bond forces, where $\mathrm{H}_{\mathbf{x1}}$ and $\mathrm{H}_{\mathbf{x2}}$ are their neighborhood horizons with the cut-off radius $\delta$.

As shown in Fig. 3, the interface bond force density between point **x1** and point **x2** can be expressed as:

$$\mathbf{f}[\mathbf{x1},t]\langle\boldsymbol{\xi}_{\mathbf{M}}\rangle = \underline{\mathbf{T}}[\mathbf{x1},t]\langle\boldsymbol{\xi}_{\mathbf{M}}\rangle - \underline{\mathbf{T}}[\mathbf{x2},t]\langle-\boldsymbol{\xi}_{\mathbf{M}}\rangle \tag{13}$$

Considering the Eq. (2) and the temperature variation in interface zone, the Eq. (13) can be

further expressed as:

$$\mathbf{f}\left[\mathbf{x}1,t\right]\left\langle \boldsymbol{\xi}_{\mathbf{M}}\right\rangle =\left(\underline{t_T}\left[\mathbf{x}1,t\right]\left\langle \boldsymbol{\xi}_{\mathbf{M}}\right\rangle +\underline{t_T}\left[\mathbf{x}2,t\right]\left\langle -\boldsymbol{\xi}_{\mathbf{M}}\right\rangle \right)\frac{\underline{\mathbf{Y}}\left\langle \boldsymbol{\xi}_{\mathbf{M}}\right\rangle }{\left|\underline{\mathbf{Y}}\left\langle \boldsymbol{\xi}_{\mathbf{M}}\right\rangle \right|} \tag{14}$$

where $\underline{t_T}\left[\mathbf{x}1,t\right]$ and $\underline{t_T}\left[\mathbf{x}2,t\right]$ are the force scalar states of points **x1** and **x2**, and they can be computed by Eq. (8) with their respective material properties.

Meanwhile, based on the Eq. (11), the bond energy density of this peridynamic interface bond $\boldsymbol{\xi}_{\mathbf{M}}$ can be typically written as:

$$\underline{w_T}=\frac{1}{2}\left(\underline{t_T}\left[\mathbf{x}1,t\right]\left\langle \boldsymbol{\xi}_{\mathbf{M}}\right\rangle +\underline{t'_T}\left[\mathbf{x}2,t\right]\left\langle -\boldsymbol{\xi}_{\mathbf{M}}\right\rangle \right)\cdot\underline{e_T}\left\langle \boldsymbol{\xi}_{\mathbf{M}}\right\rangle \tag{15}$$

where $\underline{e_T}\left\langle \boldsymbol{\xi}_{\mathbf{M}}\right\rangle$ is the extension scalar of this interface bond that can be obtained by Eq. (12), in which the average value of thermal expansion coefficients of two materials is utilized as:

$$\beta=\left(\beta_1+\beta_2\right)/2 \tag{16}$$

## 3. Peridynamic interface fracture model with thermomechanical effect

For an interface crack subjected to both the thermal and mechanical loads, the crack is mostly under a mixed-mode condition, and the residual thermal deformation has a significant influence on its fracture behaviors.

In this section, the mode separation of deformation state around interface crack is presented, an extended peridynamic mixed-mode bond failure criterion is then proposed for interface fracture analysis with thermomechanical effect consideration, and the peridynamic virtual crack closure technique (PD_VCCT) [42] is modified for energy release rate (ERR) and mode mixity computations.

### 3.1. Mode separation

As for a mixed-mode interface crack, the displacement state near crack tip can be analytically divided into mode I ($\mathbf{u}^{\mathrm{I}}$) and mode II ($\mathbf{u}^{\mathrm{II}}$) parts, in which the displacements $\mathbf{u}^{\mathrm{I}}$ and $\mathbf{u}^{\mathrm{II}}$ are symmetric and antisymmetric with respect to crack surface [71]. Thus, as shown in Fig. 4, the displacement state $\mathbf{u}_A$ of point $\mathbf{x}_A$ can be expressed with the displacement of point $\mathbf{x}_B$ as:

$$\mathbf{u}_A=\mathbf{u}_A^{\mathrm{I}}+\mathbf{u}_A^{\mathrm{II}}=\frac{1}{2}\begin{Bmatrix}u_{1A}+u_{1B}\\ u_{2A}-u_{2B}\end{Bmatrix}+\frac{1}{2}\begin{Bmatrix}u_{1A}-u_{1B}\\ u_{2A}+u_{2B}\end{Bmatrix} \tag{17}$$

where point $\mathbf{x}_B$ is the mirror symmetric point of $\mathbf{x}_A$ with respect to crack surface $x_1$, $u_{iA}$ and $u_{iB}$

are the displacement components of points $\mathbf{x}_A$ and $\mathbf{x}_B$ in axis of $x_i$ ($i$ = 1, 2). If the interface crack does not coincide with global coordinate system, the coordinate transformation from $X_1$-$X_2$ to $x_1$-$x_2$ should be applied.

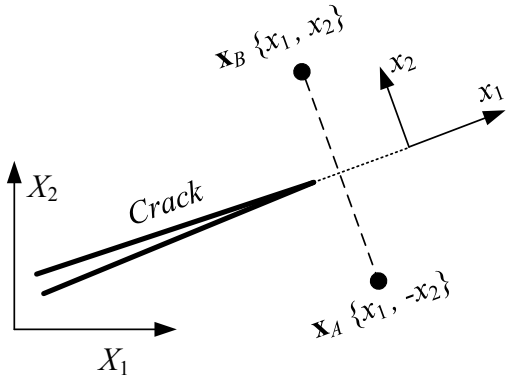


**Fig. 4.** Mirror points $\mathbf{x}_A$ and $\mathbf{x}_B$ respect to $x_1$ axis (crack surface) near crack tip, where the local coordinate system $x_1$-$x_2$ is related to crack surface, and $X_1$-$X_2$ is the global coordinate system.

Using the divided deformation states of mode I displacement ($\mathbf{u}^{\mathrm{I}}$) and mode II displacement ($\mathbf{u}^{\mathrm{II}}$), the interface bond extension, force and energy density states for the mode I and mode II parts can be respectively calculated. Since the temperature variation has no effect on mode II part displacement (shear deformation), the thermomechanical effect can only be considered for these states computation in mode I part. And the expressions of bond energy density from mode I and mode II deformations take the forms of:

$$\begin{cases} \underline{w_T}^{\mathrm{I}}\langle\boldsymbol{\xi}_{\mathbf{M}}\rangle = \dfrac{1}{2}\left(\underline{t_T}^{\mathrm{I}}\langle\boldsymbol{\xi}_{\mathbf{M}}\rangle + \left(\underline{t'_T}\right)^{\mathrm{I}}\langle-\boldsymbol{\xi}_{\mathbf{M}}\rangle\right)\cdot\underline{e_T}^{\mathrm{I}}\langle\boldsymbol{\xi}_{\mathbf{M}}\rangle \\ \underline{w}^{\mathrm{II}}\langle\boldsymbol{\xi}_{\mathbf{M}}\rangle = \dfrac{1}{2}\left(\underline{t}^{\mathrm{II}}\langle\boldsymbol{\xi}_{\mathbf{M}}\rangle + \left(\underline{t'}\right)^{\mathrm{II}}\langle-\boldsymbol{\xi}_{\mathbf{M}}\rangle\right)\cdot\underline{e}^{\mathrm{II}}\langle\boldsymbol{\xi}_{\mathbf{M}}\rangle \end{cases} \tag{18}$$

where $\underline{t_T}^{\mathrm{I}}$ and $\left(\underline{t'_T}\right)^{\mathrm{I}}$ are mode I force scaler states computed with peridynamic thermomechanical model of Eq. (8) with the separated mode I displacement ($\mathbf{u}^{\mathrm{I}}$), while $\underline{t}^{\mathrm{II}}$ and $\left(\underline{t'}\right)^{\mathrm{II}}$ are mode II force scaler states computed from Eq. (9) with the mode II displacement ($\mathbf{u}^{\mathrm{II}}$).

However, the displacement separation method can only be analytically utilized if the elastic material properties across the crack surface are same. For the bimaterial interface cracks, the material mismatch exits across the interface crack, the displacement cannot be analytically divided. But when the bimaterial ratio of $E_1$ / $E_2$ is close to 1.0, this mode separation method

can still be approximately utilized.

### 3.2. Bond failure model for mixed-mode interface cracks

Recently, a new peridynamic mixed-mode bond failure model was proposed by the authors [35] for interface delamination analysis. In present work, the mentioned model is extended for interface fracture analysis with the thermal effect consideration.

For failure perdiction of the interface bond $\boldsymbol{\xi}_{\mathbf{M}}$, the critical energy density-based power law bond failure criterion is typically utilized as:

$$\left(\frac{\underline{w}_T^{\mathrm{I}}}{\underline{w}_{\mathrm{I}c}}\right)+\left(\frac{\underline{w}^{\mathrm{II}}}{\underline{w}_{\mathrm{II}c}}\right)>1 \tag{19}$$

where $\underline{w}_T^{\mathrm{I}}$ and $\underline{w}^{\mathrm{II}}$ are the bond energy densities of the interface bonds for mode I and mode II states, which are calculated from Eq. (18). $\underline{w}_{\mathrm{I}c}$ and $\underline{w}_{\mathrm{II}c}$ are the critical bond energy density obtained from the fracture energy equivalence as:

$$\underline{w}_{\mathrm{I}c}\left\langle\boldsymbol{\xi}_{\mathbf{M}}\right\rangle=\begin{cases}\dfrac{4G_{\mathrm{I}c}}{\pi\delta^4} & \mathrm{3D}\\ \dfrac{3G_{\mathrm{I}c}}{2\delta^3 B} & \mathrm{2D}\end{cases},\quad \underline{w}_{\mathrm{II}c}\left\langle\boldsymbol{\xi}_{\mathbf{M}}\right\rangle=\begin{cases}\dfrac{48G_{\mathrm{II}c}}{\pi\delta^4}\sin^2\phi\cos^2\phi\sin^2\vartheta & \mathrm{3D}\\ \dfrac{45G_{\mathrm{II}c}}{4\delta^3 B}\sin^2\phi\cos^2\phi & \mathrm{2D}\end{cases} \tag{20}$$

where $G_{\mathrm{I}c}$ and $G_{\mathrm{II}c}$ are the mode I and mode II critical energy release rates of the material interface, $B$ is the thickness of 2D model, $\phi$ and $\vartheta$ are the direction angles of the interface bond $\boldsymbol{\xi}_{\mathbf{M}}$ related to the global coordinate system.

Thus, the bond failure criterion for mixed-mode interface crack is given. When the bond energy density of the interface bond $\boldsymbol{\xi}_{\mathbf{M}}$ grows to satisfy Eq. (19), this bond permanently breaks.

### 3.3. Energy release rate (ERR) and mode mixity of interface cracks

The energy release rate (ERR) and mode mixity are essential parameters to characterize an interface crack, and the peridynamic virtual crack closure technique (PD_VCCT) is modified for their value calculation with thermal consideration.

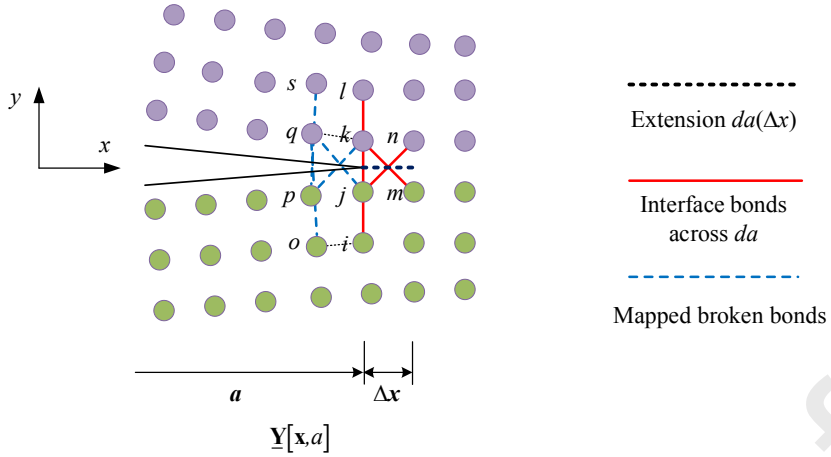


**Fig. 5.** Virtual crack closure technique in discrete peridynamic model. The interface bonds across the crack extension *da* maps to its corresponding bonds behind (e.g., the bond between nodes $\mathbf{x}_p$ to $\mathbf{x}_k$ (blue dashed line) is the mapped broken bond of interface bond between points $\mathbf{x}_j$ to $\mathbf{x}_n$ (red line)).

As shown in Fig. 5, the numerical mode I and mode II energy release rates of an interface crack with the thermal consideration can be expressed as:

$$\begin{cases} \overline{G}_{\mathrm{I}}(a) = \dfrac{1}{\Delta x} \displaystyle\sum_{\boldsymbol{\xi}_{ik} \in \mathrm{S}_{\boldsymbol{\xi}}, \boldsymbol{\xi}_{ik} \to \boldsymbol{\xi}_{oq}} \left( \frac{1}{2} \left\{ \underline{t}_T^{\,\mathrm{I}} \langle \mathbf{x}_k - \mathbf{x}_i \rangle + \left( \underline{t}'_T \right)^{\mathrm{I}} \langle \mathbf{x}_i - \mathbf{x}_k \rangle \right\} \cdot \underline{e}_T^{\,\mathrm{I}} \langle \mathbf{x}_q - \mathbf{x}_o \rangle \right) V_i V_k \\ \overline{G}_{\mathrm{II}}(a) = \dfrac{1}{\Delta x} \displaystyle\sum_{\boldsymbol{\xi}_{ik} \in \mathrm{S}_{\boldsymbol{\xi}}, \boldsymbol{\xi}_{ik} \to \boldsymbol{\xi}_{oq}} \left( \frac{1}{2} \left\{ \underline{t}^{\mathrm{II}} \langle \mathbf{x}_k - \mathbf{x}_i \rangle + \left( \underline{t}' \right)^{\mathrm{II}} \langle \mathbf{x}_i - \mathbf{x}_k \rangle \right\} \cdot \underline{e}^{\mathrm{II}} \langle \mathbf{x}_q - \mathbf{x}_o \rangle \right) V_i V_k \end{cases} \tag{21}$$

where the discrete peridynamic numerical model is considered, $\Delta x$ is the crack extension length, $\mathrm{S}_{\boldsymbol{\xi}}$ is the set of all interface bonds across the crack extension *da*, $\boldsymbol{\xi}_{oq}$ is the corresponding bond mapped of bond $\boldsymbol{\xi}_{ik}$, $V_i$ and $V_k$ are volumes of nodes $\mathbf{x}_i$ and $\mathbf{x}_k$, respectively. $\underline{e}$ is the extension scalar state, and $\underline{t}$ and $\underline{t}'$ are the force scalar states. Similarly, since the temperature variation only has influence on mode I part deformation, thermomechanical effect is only considered in separated mode I part, while it can be not considered in mode II state.

Additionally, the ERR-based mode mixity of the interface crack, $\psi_G$, can thus be defined as:

$$\tan^2 \psi_G = \frac{G_{\mathrm{II}}}{G_{\mathrm{I}}} \tag{22}$$

Because of the material mismatch across the interface crack, the ERRs of $G_{\mathrm{I}}$ and $G_{\mathrm{II}}$, and the mode mixity $\psi_G$ do not have unique values. They depend on the mesh size $\Delta x$ and do not converge as $\Delta x$ converges to infinitesimal value. However, the value of total energy release

rate is still unique, and the mesh-independent mode mixity $\psi$ can be computed with $\psi_G$ by the correction method in [72].

## 4. Peridynamic contact model for frictional fracture

When the residual thermal deformation exists in the material interface zone, compressive stress would occur along a fracture surface, and it results in normal contact and frictional tangential slip between two crack surfaces. Here, a simple node to node peridynamic contact model is proposed to model this frictional contact, and the small tangential slip displacement is considered in the crack surface.

### 4.1. Contact between peridynamic discrete models

In crack surface, two discrete peridynamic models of material 1 and material 2 are shown in Fig. 6(a). With the uniform grid mesh size, the node to node contact maps are identified as the peridynamic contact bonds $\overline{\boldsymbol{\xi}}$, in which the overline is used for distinguishing to the original bonds. For example, as shown in Fig. 6(b), nodes $\mathbf{x}_i$ and $\mathbf{x}_j$ are connected by the contact bond $\overline{\boldsymbol{\xi}}_{ij}$, where $\mathbf{x}_i$ and $\mathbf{x}_j$ are defined as the outermost nodes that belong to material 1 and material 2, respectively. Since the basic contact condition is that no material overlap can occur, the contact in peridynamic models happens when:

$$\left(\mathbf{y}_i-\mathbf{y}_j\right)\cdot\mathbf{n}<\Delta x \tag{23}$$

where $\mathbf{y}_i$ and $\mathbf{y}_j$ are the deformed vectors of boundary nodes $\mathbf{x}_i$ and $\mathbf{x}_j$, $\mathbf{n}$ is the unit normal vector of the contact surface, and $\Delta x$ is the uniform grid size.

When the contact happens, the contact bond $\overline{\boldsymbol{\xi}}_{ij}$ deforms from $\underline{\mathbf{X}}\langle\overline{\boldsymbol{\xi}}_{ij}\rangle$ to $\underline{\mathbf{Y}}\langle\overline{\boldsymbol{\xi}}_{ij}\rangle$, and the bond normal stretch $\underline{s}_n$ is defined as:

$$\underline{s}_n\langle\overline{\boldsymbol{\xi}}_{ij}\rangle=\frac{\left|\underline{\mathbf{Y}}\langle\overline{\boldsymbol{\xi}}_{ij}\rangle\cdot\mathbf{n}\right|-\left|\underline{\mathbf{X}}\langle\overline{\boldsymbol{\xi}}_{ij}\rangle\cdot\mathbf{n}\right|}{\left|\underline{\mathbf{X}}\langle\overline{\boldsymbol{\xi}}_{ij}\rangle\cdot\mathbf{n}\right|} \tag{24}$$

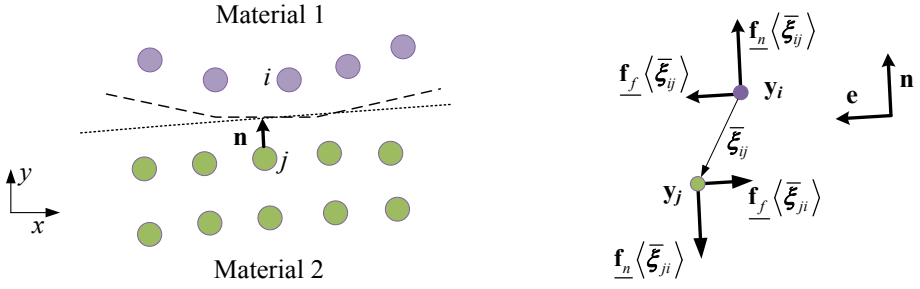

(a) (b)

**Fig. 6.** Discrete peridynamic contact model: (a) node to node contact maps in contact surface (e.g., the contact map between nodes $\mathbf{x}_i$ and $\mathbf{x}_j$), and (b) the peridynamic frictional contact bond force densities between nodes $\mathbf{x}_i$ and $\mathbf{x}_j$.

### 4.2. Peridynamic contact bond force density

Thus, as shown in Fig. 6(b), the peridynamic normal and tangential contact bond force densities are respectively defined as:

$$\underline{\mathbf{f}}_n\left\langle \overline{\boldsymbol{\xi}}_{ij}\right\rangle = -c_n \underline{s}_n \left\langle \overline{\boldsymbol{\xi}}_{ij}\right\rangle \mathbf{n} \tag{25}$$

$$\underline{\mathbf{f}}_f\left\langle \overline{\boldsymbol{\xi}}_{ij}\right\rangle = f\left|\underline{\mathbf{f}}_n\left\langle \overline{\boldsymbol{\xi}}_{ij}\right\rangle\right|\mathbf{e} \tag{26}$$

where $f$ is the frictional coefficient, $\mathbf{n}$ and $\mathbf{e}$ are the unit normal and tangential vectors of the contact surface, in which $\mathbf{e}$ is inversed to the sliding direction. $c_n$ is the contact micromodulus of the peridynamic contact bond, it can be expressed in two-dimensional (2D) case as:

$$c_n = \frac{E_c}{(\Delta x)^3 B},\quad \frac{2}{E_c} = \frac{1}{E_1} + \frac{1}{E_2} \tag{27}$$

where $\Delta x$ is uniform grid size, $B$ is the thickness of 2D model, and $E_1$ and $E_2$ are the elastic modulus of the material 1 and material 2.

Thus, in this node to node sliding frictional contact, the bond normal stretch $\underline{s}_n$ is computed and the bond deformation in the tangential vector has no contribution to the contact bond forces. Additionally, the contact bond force density is restricted by the Newton's Third law as:

$$\underline{\mathbf{f}}\left\langle \overline{\boldsymbol{\xi}}_{ij}\right\rangle = -\underline{\mathbf{f}}\left\langle \overline{\boldsymbol{\xi}}_{ji}\right\rangle \tag{28}$$

Meanwhile, the criterion for contact condition evaluation should be defined for whether a crack surface is in contact. The contact criterion is given in Eq. (23). For any node maps along the crack surface, when the contact bond $\overline{\boldsymbol{\xi}}_{ij}$ deform to satisfy Eq. (23), the involving nodes are in contact, the peridynamic bond force density for bond $\overline{\boldsymbol{\xi}}_{ij}$ would be applied as:

$$\underline{\mathbf{f}}\left\langle \overline{\boldsymbol{\xi}}_{ij}\right\rangle = \underline{\mathbf{f}}_n\left\langle \overline{\boldsymbol{\xi}}_{ij}\right\rangle + \underline{\mathbf{f}}_f\left\langle \overline{\boldsymbol{\xi}}_{ij}\right\rangle \tag{29}$$

While when the direction of normal contact force is inversed as:

$$\underline{\mathbf{f}}_n\left\langle\overline{\boldsymbol{\xi}}_{ij}\right\rangle\cdot\mathbf{n}<0 \tag{30}$$

The contact should be released, and the normal and tangential peridynamic contact bond forces are all set to zero.

## 5. Examples

In the section, three examples, .i.e. the single edge-notched bimaterial (SENB) plate, asymmetric bimaterial cantilever beams (ABCB), and four points bend (FPB) specimens under the mechanical and thermal loads are presented for the proposed peridynamic models verification and application.

### 5.1. Single edge-notched bimaterial (SENB) plate

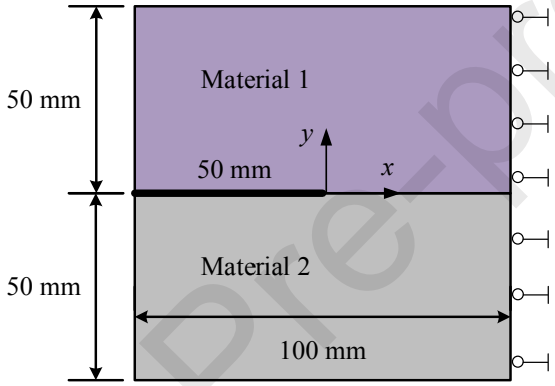


**Fig. 7.** The single edge-notched bimaterial (SENB) plate under uniform thermal loading.

The single edge-notched bimaterial (SENB) plate with uniform thermal loading is first studied. As shown in Fig. 7, the geometry sizes of the SENB plate are presented, in which a middle crack exits along the material interface, the boundary condition is $u_x = 0$ at the right edge. Both the plane stress and plane strain conditions are considered and the uniform thickness of 1 mm is utilized. The uniform temperature variation of $\Delta T$ = -100 ℃ is applied on the SENB plate. And elastic isotropic material 1 and material 2 are considered on the upper and lower sides of the interface, and material parameters are given in Table 1.

For peridynamic bimaterial modeling, uniform mesh size is used. The $\delta$-convergence analysis [73] is performed with decreasing horizon values of $\delta$ = 4 mm, 2 mm and 1 mm, and a fixed value of $m$ = 4. The peridynamic thermomechanical model of Eq. (8) is utilized for elastic behaviors analysis of this bimaterial plate. In the crack surface, the peridynamic contact model of Eq. (25) is utilized for frictional contact modeling, and the frictionless condition with the frictional coefficient value of $f$ = 0 is considered. The peridynamic virtual crack closure

technique (PD_VCCT) in Eq. (21) is considered for the energy release rate (ERR) computation of the interface crack. The adaptive dynamic relaxation (ADR) method [74] is performed for quasi-static analysis. The FEM solutions are also presented for the sake of comparison and validation, in which the 4-node bilinear mesh with uniform grid size of 1mm is utilized.

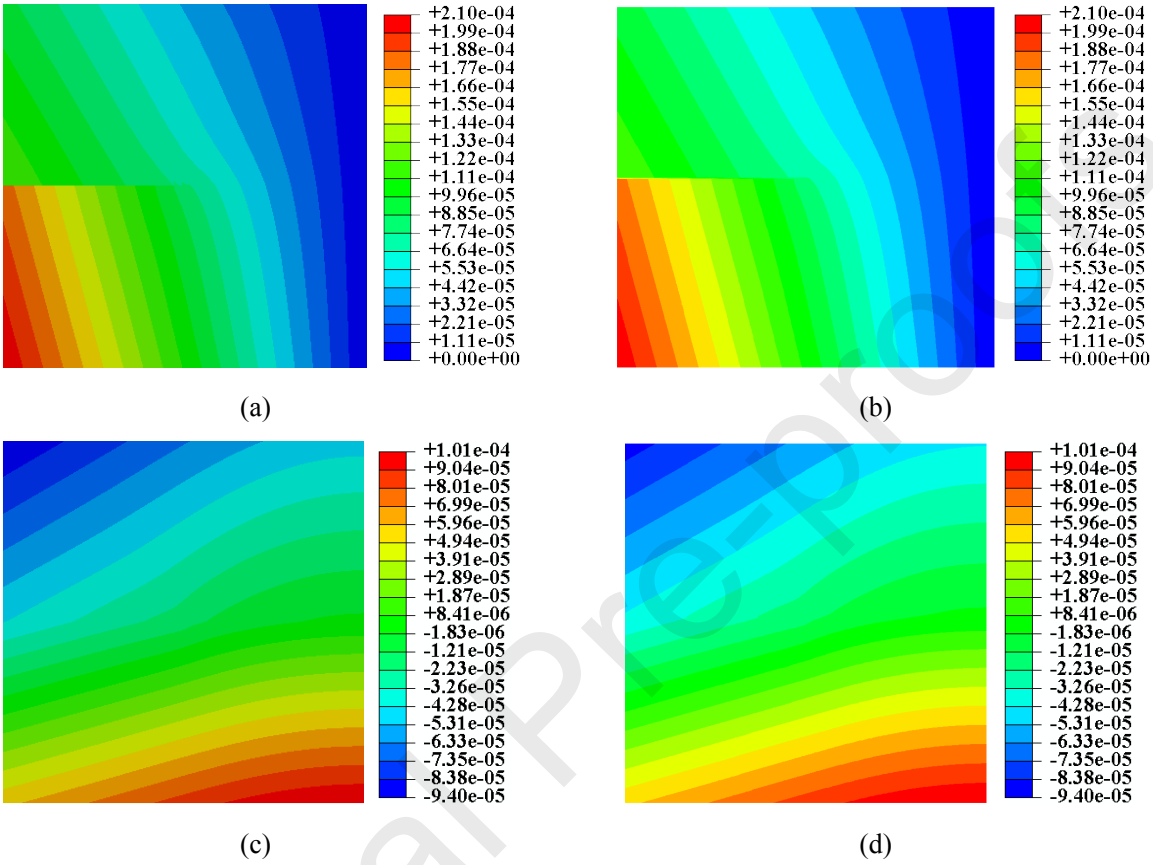


**Fig. 8.** Displacements of the SENB plate in *x*-direction: (a) FEM and (b) Peridynamics, and *y*-direction: (c) FEM and (d) peridynamics with temperature variation of -100 ℃ in the plane stress condition (m).

Comparisons of displacement distributions of the SENB plate from the present peridynamic model and the FEM are given in Fig. 8, where fixed values of $\delta$ = 1 mm and $m$ = 4 with the plane stress condition are considered. As shown in Fig. 8, the displacements from the present model greatly match those from the FEM solutions. For the quantitative comparison, displacement components along the lines of $x$ = -20 mm and $x$ = 20 mm are presented in Fig. 9; while the volume dilatation (defined in Eq. (5)) along the line of $x$ = 20 mm is presented in Fig. 10, where horizon values of $\delta$ = 4 mm, 2 mm and 1 mm, and a fixed value of $m$ = 4 are considered for the $\delta$-convergence. Generally, it is shown that the solutions predicted by presented peridynamic model are converging to the FEM solutions as nonlocal horizon $\delta$ decreases, in both the plane stress and plane strain cases. Additionally, the curves from

peridynamics are smoother than the FEM solutions (see Fig. 10), which shows the smearing effect of nonlocal peridynamic interface model on elastic property [70]. Typically, along the line $x$ = -20 mm (see Fig. 9(a)), the $x$-directional displacement is discontinuous across the crack surface which means that the sliding frictional contact is presented.

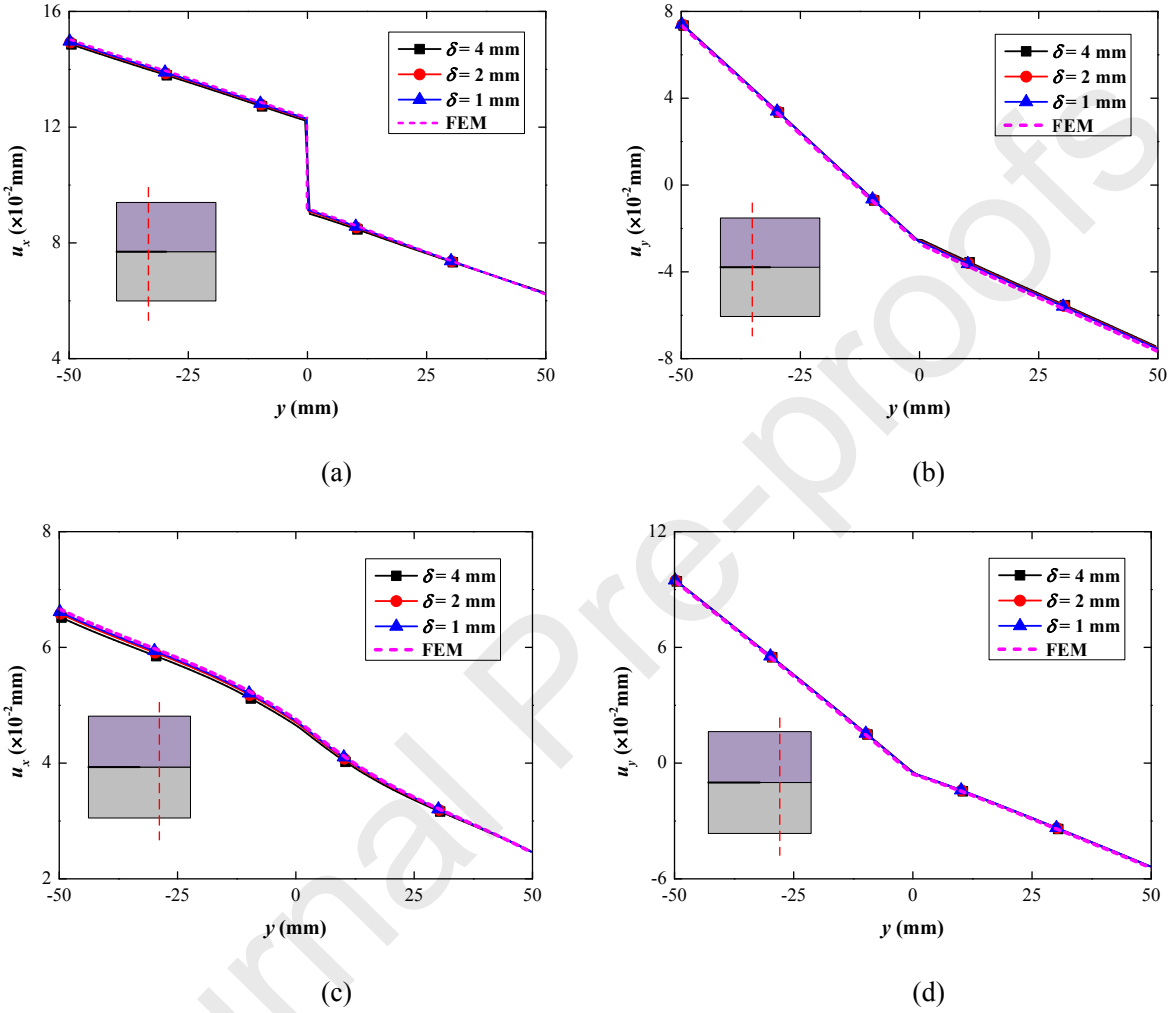


**Fig. 9.** Displacements with different values of $\delta$ along the lines of $x$ = -20 mm: (a) $x$ component, and (b) $y$ component, and $x$ = 20 mm: (c) $x$ component, and (d) $y$ component in the plane stress condition.

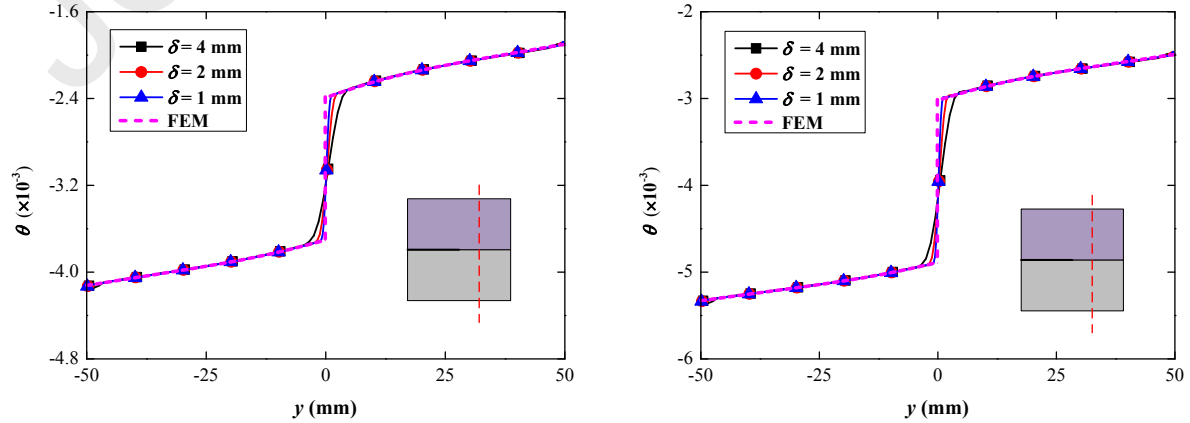

(a) (b)

**Fig. 10.** The volume dilatation along the line of $x$ = 20 mm with different values of $\delta$ in the plane stress (a) and plane strain (b) cases.

The ERR values of the interface crack are then computed by the PD_VCCT method and compared to the FEM solution, which are reported in Table 2. As shown, when the temperature variation is considered, the interface crack is under pure mode II condition. And both for the plane stress and plane strain conditions, the ERR values from the peridynamic model are converging to the FEM solutions as nonlocal horizon $\delta$ decreases, with the maximum differences of 1.0 % and 1.8 %, respectively.

**Table 1. Elastic properties of two materials**

| Material | Elastic modulus $E$ (GPa) | Poisson's ratio $v$ | Density $\rho$ (kg/m$^3$) | Thermal exp. coeff. $\beta$ ($10^{-6}$/°C) |
|---|---|---|---|---|
| Material 1 | 100 | 0.30 | 3000 | 10 |
| Material 2 | 200 | 0.30 | 3000 | 20 |

**Table 2. Energy release rate of SENB plate with the temperature variation of -100 ℃**

| | Plane stress | | | | Plane strain | | | |
|---|---|---|---|---|---|---|---|---|
| $\delta$ (mm) | 4 | 2 | 1 | FEM | 4 | 2 | 1 | FEM |
| $G_{II}$ (J/m$^2$) | 456.91 | 451.57 | 447.43 | 452.23 | 887.05 | 855.99 | 838.02 | 839.50 |

**5.2.** Asymmetric bimaterial cantilever beams (ABCB)

The asymmetric bimaterial cantilever beam (ABCB) specimen subjected to both the mechanical and thermal loads are investigated, where the geometrical sizes, loading and boundary conditions are presented in Fig. 11. A preset crack $a_0$ exists along the bimaterial interface. And the plane stress condition is considered with the uniform beam thickness of $B$ = 1 mm. The elastic isotropic materials are used, and the material parameters are reported in Table 3. In the material interface, the interfacial fracture toughness of $G_I$ = 800 J/m$^2$ and $G_{II}$ = 2000 J/m$^2$ are considered for interface crack modeling. And the frictional contact exists along the crack surface with the frictional coefficient values of $f$ = 0.0 or $f$ = 0.3. In the numerical peridynamic model, the uniform grid size is considered. The adaptive dynamic relaxation

(ADR) method [74] is performed for quasi-static analysis; while the explicit time integration is applied for the fracture analysis, and critical time steps for different mesh sizes can be obtained from [19]. The FEM method is also considered for the result comparison and model verification, and the 4-node bilinear mesh with uniform grid size of 1mm is used.

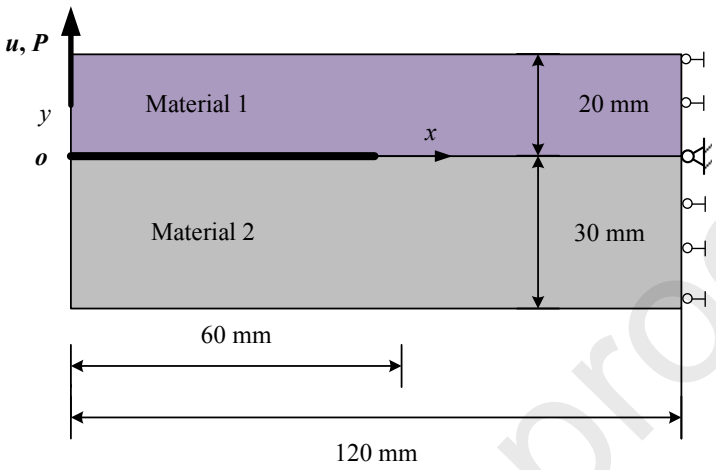


**Fig. 11.** Asymmetric bimaterial cantilever beams (ABCB) with an interface crack.

**Table 3. Material properties of two plates**

| Material | Elastic modulus $E$ (GPa) | Poisson's ratio $\nu$ | Density $\rho$ (kg/m$^3$) | Thermal exp. coeff. $\beta$ ($10^{-6}$/°C) |
|---|---|---|---|---|
| Material 1 | 207 | 0.312 | 8900 | 15.5 |
| Material 2 | 340 | 0.310 | 3920 | 23.0 |

*5.2.1 Elastic behaviors with uniform thermal load*

First, the ABCB specimen under the temperature variation of $\Delta T$ = -100 ℃ is considered. For elastic behaviors modeling, the peridynamic thermomechanical model of Eq. (8) is utilized. And the peridynamic contact model of Eqs. (25) and (26) is utilized on the crack surface for frictional contact modeling.

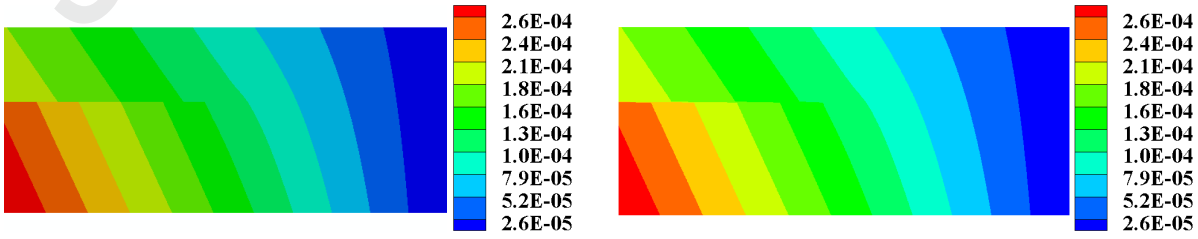


(a) (b)

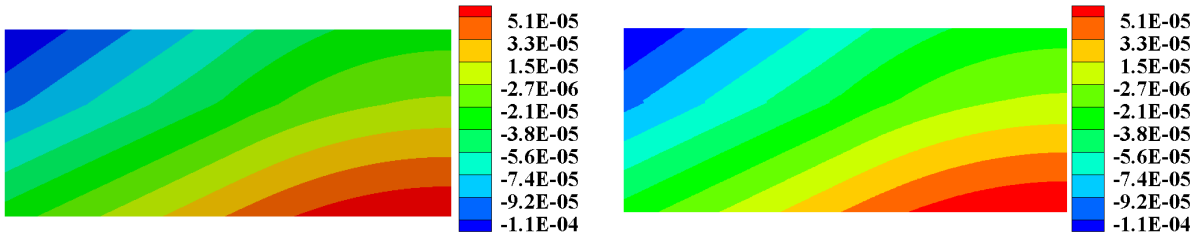


(c) (d)

**Fig. 12.** Comparisons of displacement distributions in $x$-direction: (a) FEM and (b) Peridynamics, and $y$-direction: (c) FEM and (d) peridynamics of the ABCB specimen in case of $f = 0.3$ (m).

As shown in Fig. 12, displacement distributions of the ABCB plate from the peridynamic thermomechanical model and the FEM are presented, where fixed values of $\delta = 1$ mm and $m = 4$ with the plane stress condition are considered, and the frictional coefficient values of $f = 0.3$ is considered. While the displacements and volume dilatation along the line of $x = 80$ mm are typically shown in Fig. 13, where horizon values of $\delta = 4$ mm, 2 mm and 1 mm, and a fixed value of $m = 4$ are considered for the $\delta$-convergence. Apparently, the comparisons between the peridynamic and FEM solutions shows that the peridynamic thermomechanical and contact models successfully capture the elastic material behaviors of ABCB specimen.

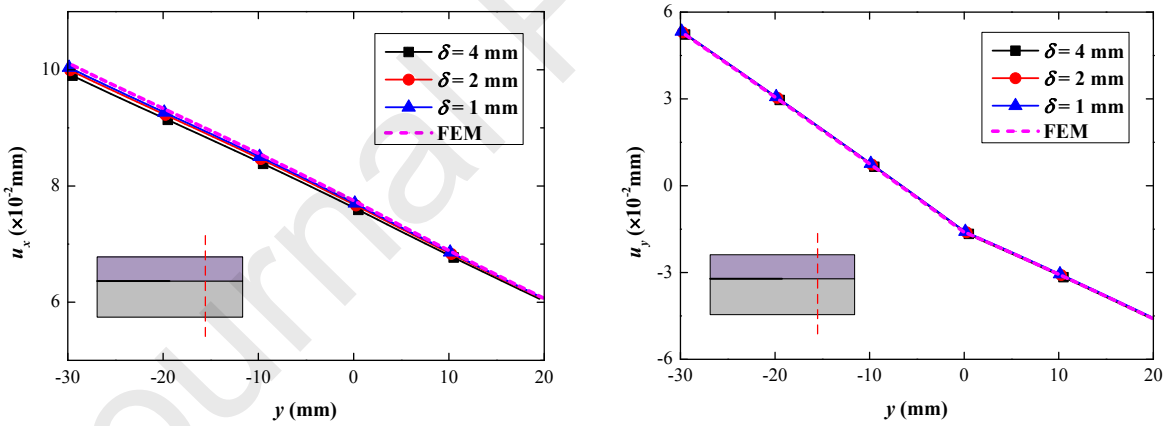


(a) (b)

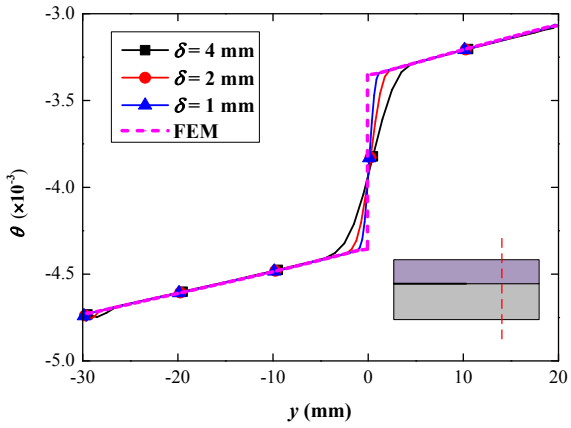


(c)

**Fig. 13.** Displacements and volume dilatation with different values of $\delta$ along the line of $x$ = 80 mm with the frictional coefficient of $f$ = 0.3: (a) $x$ component, (b) $y$ component displacements, and (c) volume dilatation.

Meanwhile, as reported in Table 4, the ERR values of the interface crack are computed by the PD_VCCT method and compared to the FEM solution, in which the frictional coefficient values of $f$ = 0.0 and $f$ = 0.3 are respectively utilized. As shown in Table 4, when the frictional contact is considered along the crack surface, the ERR values are smaller than the frictionless case ($f$ = 0.0). Since the direction of frictional force is inversed to the sliding direction, the friction along the crack surface has the opposite effect on the shear deformation, which leads to the smaller value of mode II ERR. Additionally, the predicted ERR values are closely to the FEM solutions both in cases of $f$ = 0.0 and $f$ = 0.3, within the differences of 1.0 % and 2.5 %, respectively.

**Table 4. Energy release rate of ABCB specimen with the temperature variation of -100 ℃**

| | $f$ = 0.0 | | | | $f$ = 0.3 | | | |
|---|---|---|---|---|---|---|---|---|
| $\delta$ (mm) | 4 | 2 | 1 | FEM | 4 | 2 | 1 | FEM |
| $G_{II}$ (J/m$^2$) | 288.15 | 281.10 | 276.80 | 273.30 | 239.98 | 236.74 | 236.0 | 242.10 |

*5.2.2 Frictional fracture of interface crack during cooling*

Then, the cooling temperature of $\Delta T(t) = -1.0\times10^5 * t$ ℃ is applied on the ABCB specimen for interface delamination analysis. For interface fracture modeling, the proposed peridynamic bond failure model in Eq. (19) is utilized.

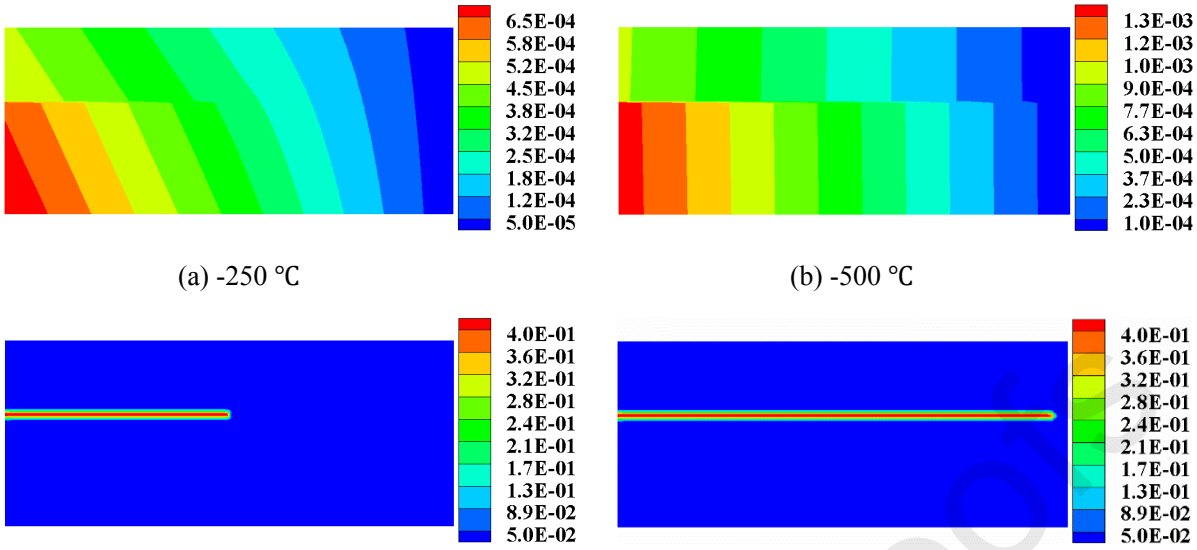


(a) -250 ℃ (b) -500 ℃

(c) -250 ℃ (d) -500 ℃

**Fig. 14.** Distributions of *x*-direction displacement (m) [(a) and (b)], and nonlocal damage [(c) and (d)] at the typical temperature variations of -250 ℃ and -500 ℃.

The distributions of *x*-direction displacement and nonlocal damage (crack path) of the ABCB specimen at the typical temperature variations of -250 ℃ and -500 ℃ are presented in Fig. 14, where the frictional coefficient of $f = 0.3$ is considered. With the cooling temperature variation, the shear-dominated deformation appears along the material interface (see Fig. 14(a)), and the crack starts to grow from the pre-crack tip (see Fig. 14(c)) and propagates along the bimaterial interface (see Fig. 14(d)).

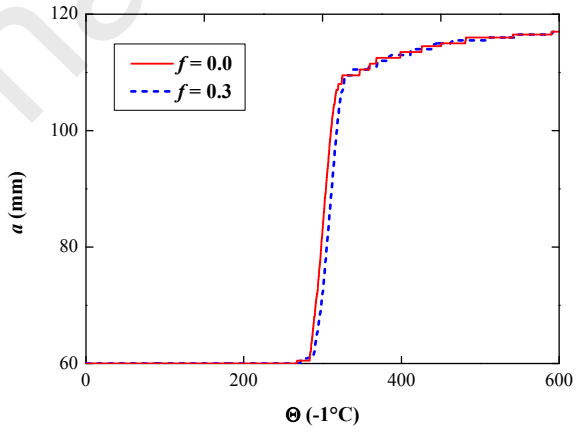


**Fig. 15.** Crack lengths of the ABCB specimens with the cooling temperature in cases of $f = 0.0$ and $f = 0.3$.

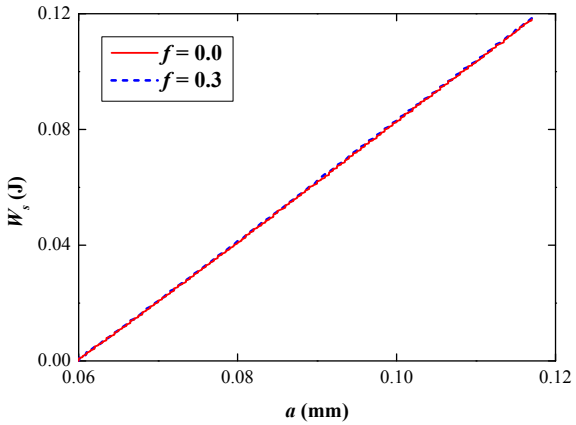


**Fig. 16.** Incremental surface energy related to crack length during ABCB interface crack growth in cases of $f = 0.0$ and $f = 0.3$.

Meanwhile, crack lengths of the ABCB specimens with the cooling temperature variation are presented in Fig. 15, in which the frictional coefficients of $f = 0.0$ and $f = 0.3$ are respectively considered. As shown in Fig. 15, the interface cracks start to grow at the typical temperature variations of -283 ℃ and -289 ℃ in the cases of $f = 0.0$ and $f = 0.3$, and the differences of them to the FEM solutions (i.e., -271 ℃ and -287 ℃) are 4.6 % and 0.5 %, respectively. The curves also show that the friction on crack surface have a negative effect on the interface delamination. In addition, the plots of the total incremental surface energy $W_S$ related to the crack length $a$ are shown in Fig. 16. The nearly coincident curves show that the numerical released energy have the same slope in frictionless ($f = 0.0$) and frictional ($f = 0.3$) cases.

*5.2.3 Energy release rates with coupled loads*

The coupled thermal and mechanical loads are then applied to the ABCB specimen (see Fig. 11) to investigate the effect of residual thermal on the interface fracture behaviors.

Here, two loading cases are performed. In case 1, the loading conditions of $u = -1.0 \times 10^{-3}$ m and $\Delta T = 0$ ℃ are considered; while in case 2, $u = -1.0 \times 10^{-3}$ m and $\Delta T = -100$ ℃ are applied. Thus, cases 1 and 2 are regarded as conditions with or without thermal effects. In these cases, the energy release rates (ERRs) and mode mixity of interface cracks are computed by the PD_VCCT-based method in Eqs. (21) and (22), and compared to the FEM solutions for comparison.

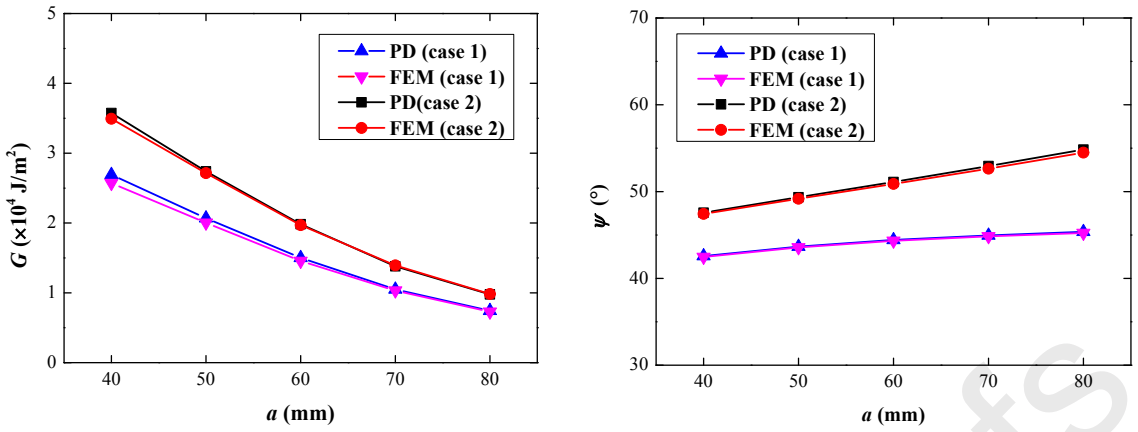


**Fig. 17.** The total energy release rate (a) and mode mixity (b) of the ABCB specimens with varying values of pre-crack length under case1 and case 2 loading conditions: case 1 for $u$ = -1.0 × $10^{-3}$ m and $\Delta T$ = 0 ℃, while case 2 for $u$ = -1.0 × $10^{-3}$ m and $\Delta T$ = -100 ℃.

The ERRs and mode mixity of the ABCB specimens in above two loading cases are presented in Fig. 17, where the varying pre-crack lengths from 40 mm to 80 mm are considered. As shown in Fig. 17, the interface cracks are under mixed mode conditions in both two cases, and the residual thermal load can largely increase the values of total ERR and mode mixity of the interface cracks. Typically, when the interface crack is under coupled loads (case 2), the total ERR includes three terms as [8]:

$$G = G_m + G_{th} + G_{\text{add}} \tag{31}$$

where $G_m$ is the ERR induced by the mechanical load (case 1), $G_{th}$ is the ERR from the thermal load (see Table 4), and $G_{\text{add}}$ is the work of the mechanical forces in the residual displacement field. Meanwhile, the predicted values of the total ERR and mode mixity from peridynamic model have a great agreement to the FEM solutions, within the maximum differences of 2.3 % and 4.6 % in cases 1 and 2, respectively.

*5.2.4 Interface fracture with coupled loads*

The interface fracture with coupled loads is then investigated, in which the ABCB specimen is subjected to increasing displacement of $u(t)$ = 5.0 × $10^{-2}$ * $t$ m (see Fig. 11), and the fixed temperature variations of $\Delta T$ = -100 ℃ and -200 ℃ are respectively considered as the residual thermal conditions. For interface fracture analysis, the peridynamic bond failure model in Eq. (19) is performed for the mixed mode interface bond failure prediction.

The distributions of $y$-direction displacement, and crack path of the ABCB specimen at the typical loading displacements are presented in Fig. 18, where the fixed temperature variation of $\Delta T$ = -100 ℃ is considered and the frictional coefficient value of $f$ = 0.0 is utilized. Since the residual deformation exists at the ABCB specimen, the loading displacement starts with $u_0$ = -9.7×10$^{-5}$ m, rather than zero (see Fig. 18(a)). With the increasing displacement loading, the interface crack starts to grow when $u$ = 1.5×10$^{-4}$ m (see Fig. 18(c)), and propagates along the interface (see Fig. 18(f)). Typically, as shown in Figs. 18(c) and (e), the upper loading displacement plays a gradually important role on interface fracture.

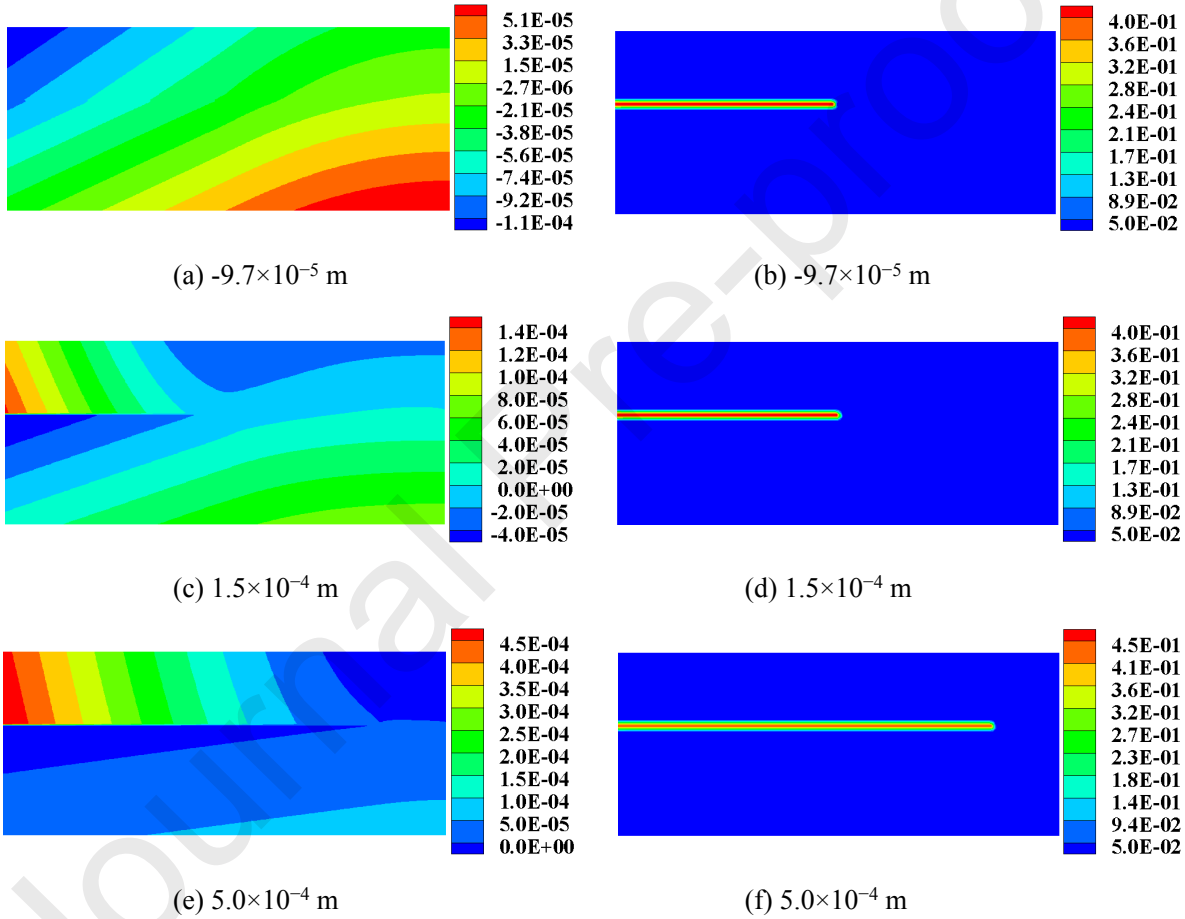


(a) -9.7×10$^{-5}$ m (b) -9.7×10$^{-5}$ m

(c) 1.5×10$^{-4}$ m (d) 1.5×10$^{-4}$ m

(e) 5.0×10$^{-4}$ m (f) 5.0×10$^{-4}$ m

**Fig. 18.** Distributions of $y$-direction displacement (m) [(a), (c) and (e)] and local damage/crack path [(b), (d) and (f)] of the ABCB specimen with temperature variation of -100 ℃ and dispalcement loads of -9.7×10$^{-5}$ m, 1.5×10$^{-4}$ m and 5.0×10$^{-4}$ m.

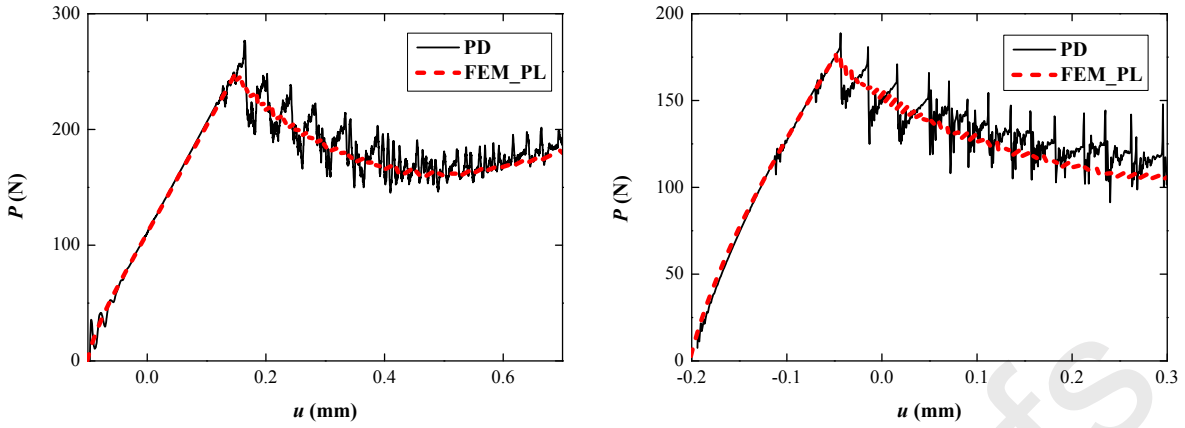


**Fig. 19.** Applied loads of the ABCB specimens with the increasing displacement loading and typical temperature variations of (a) -100 ℃ and (b) -200 ℃ by peridynamic and FEM VCCT method.

The applied load-displacement curves of ABCB specimens are shown in Fig. 19, where the fixed temperature variations of $\Delta T$ = -100 ℃ and -200 ℃ are respectively considered. For comparison, the FEM-based VCCT method with the same power-law fracture criterion is performed. As shown in Fig. 19, the curves start with the residual displacement, increase with the applied displacement load, and then drop when interface cracks start to grow. And the numerical fluctuation occurs when cracks start to grow because of the explicit time integration strategy. Generally, the peridynamic model successfully captures load-displacement relationship of the ABCB tests compared with the FEM solutions. The predicted applied loads from peridynamics are 250.12 N and 129.60 N, with the difference of 2.0 % to the FEM results (i.e., 245.95 N and 131.33 N).

*5.2.5 Interface cracks kinking*

For an interface crack, it may grow along the interface or kink out of the interface. The interface crack kinking fracture is last investigated with the additional material 1 critical energy release rate of $G_0$ = 800 J/m$^2$. The increasing displacement loading of $u(t) = 5.0 \times 10^{-2} * t$ m is applied, and the fixed temperature variations of $\Delta T$ = 0 ℃ and -100 ℃ are respectively considered. For interface crack path prediction, the failure competition between interface bonds and material bonds is applied [70], in which the bond failure model in Eq. (19) is performed for the interface bond failure prediction, while the mode I critical energy density criterion [35] is considered for material bonds.

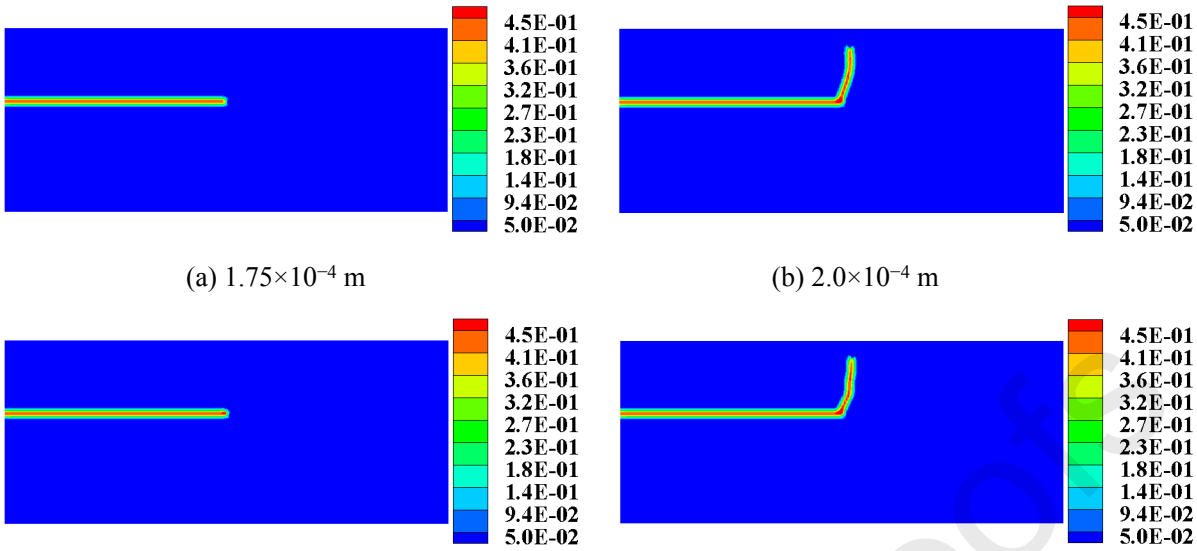


(a) $1.75\times10^{-4}$ m (b) $2.0\times10^{-4}$ m

(c) $0.25\times10^{-4}$ m (d) $1.25\times10^{-4}$ m

**Fig. 20.** Nonlocal damage (crack paths) of the ABCB specimens with the increasing displacement loading and typical temperature variations of 0 ℃ [(a) and (b)], and -100 ℃ [(c) and (d)].

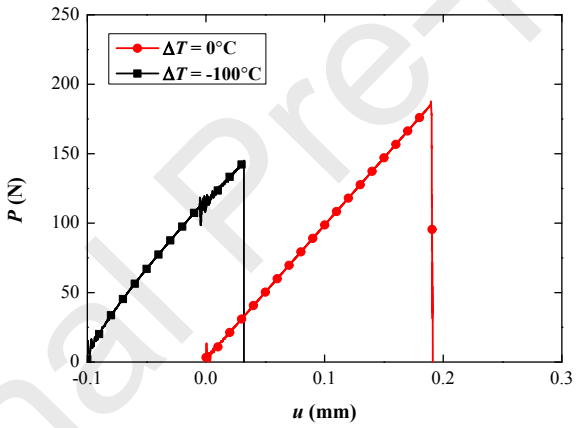


**Fig. 21.** Applied loads of the ABCB specimens with the increasing displacement loading and typical temperature variations of 0 ℃ and -100 ℃.

The crack paths of the ABCB specimens with the typical displacement loads are presented in Fig. 20, in which the temperature variations of 0 ℃ and -100 ℃ are respectively considered for the thermal effects consideration. As shown in Fig. 20, with the increasing displacement loading, the interface crack starts to grow from kinking out the interface, rather than along the interface because of the mode mixity in crack tip. The crack kinking angles are close in different temperature conditions. Additionally, the curves of applied loads with the increasing displacement loading are given in Fig. 20. As shown, compared to interface delamination curves (see Fig. 19), applied loads drop suddenly to zero when cracks kink out the interface.

And in typical case of $\Delta T$ = -100 ℃, the critical applied load is much smaller than the delamination case (compare Figs. 19(a) and 21), which means that the interface crack prefers kinking out the interface if the same values of interfacial fracture toughness of $G_I$ and material 1 critical energy release rate of $G_0$ are utilized. Meanwhile, compared to the case of $\Delta T$ = 0 ℃, the interface crack with the residual thermal effect has the smaller values of critical displacement and applied loads.

**5.3.** Four point bending (FPB) test

Last, four point bending (FPB) test of the ceramic-metal joints is investigated as shown in Fig. 22. A preset interface crack is considered with the varying length $a$. The plane stress condition is utilized, and the uniform thickness of the beams is 5 mm. The materials of $Si_3N_4$-S45C are typically considered, and the material parameters are given in Table 5. In the bonded interface, the interfacial fracture toughness of $G_I$ = 134 J/m$^2$ and $G_{II}$ = 1000 J/m$^2$ are utilized for interface fracture analysis. And the frictionless contact is considered along the crack surface.

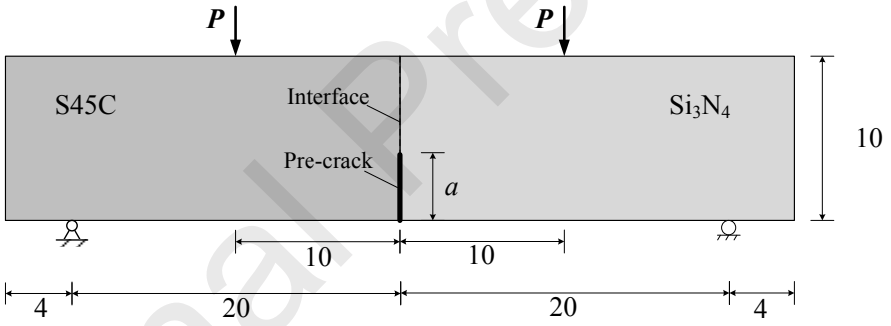


**Fig. 22.** Four points bending (FPB) specimen with an interface crack.

In numerical peridynamic model, the uniform grid mesh is used. The fixed mesh sizes of $\delta$ = 0.8 mm and $m$ = 4 are performed. The explicit time integration is applied for the fracture analysis, and critical time step is $\Delta t = 4.0 \times 10^{-8}$ s. The linearly increasing force load of $P(t)$ = $-1.6 \times 10^4 * t$ N is applied in two loading points (see Fig. 22). The fixed temperature variations of $\Delta T$ = 0 ℃ and -200 ℃ are respectively considered for the loading conditions with or without residual thermal effect. The proposed peridynamic thermomechanical model of Eq. (8), interface fracture model of Eq. (19) and crack surface contact model of Eq. (25) are utilized in this numerical test.

The applied load related to crack mouth opening displacement ($P$-CMOD) curves of the FPS tests are presented in Fig. 23, where the varying pre-crack lengths from 2 mm to 6 mm are

respectively considered, and the CMOD is calculated from the relative displacement of the two-sided points of the interface crack mouth (see Fig. 22). As shown in Fig. 23, the applied loads $P$ nearly increase linearly with the CMOD, and reach their critical values when cracks start to grow. For the smaller pre-crack length $a$, the slopes of curves are relatively higher and the crack applied loads are larger. And in the case with the residual thermal effect ($\Delta T$ = -200 ℃), the residual deformation exists, and the curves start with the residual displacements.

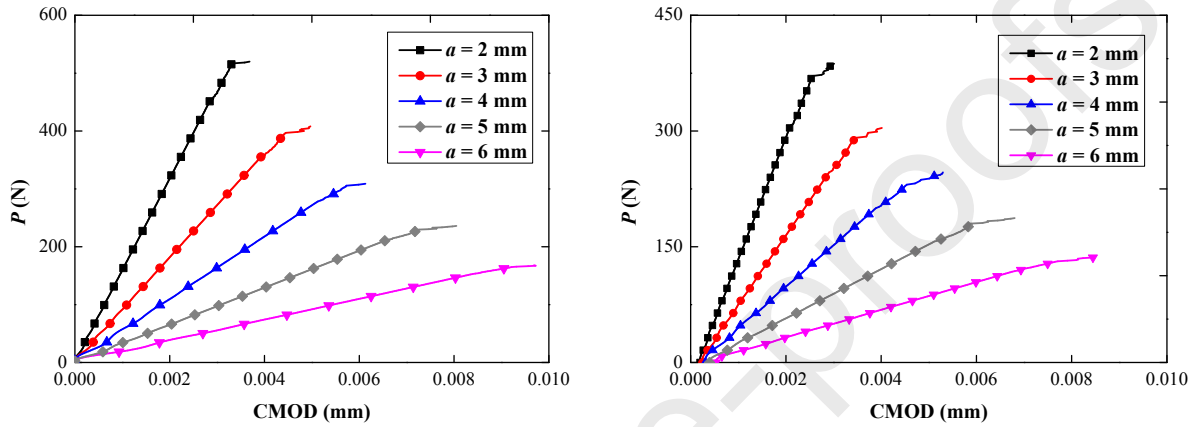


(a) (b)

**Fig. 23.** The crack mouth opening displacement (CMOD) vs applied load of the FPB specimens with the typical temperature variations of (a) 0 ℃ and (b) -200 ℃, with varying crack lengths $a$ from 2 mm to 6 mm.

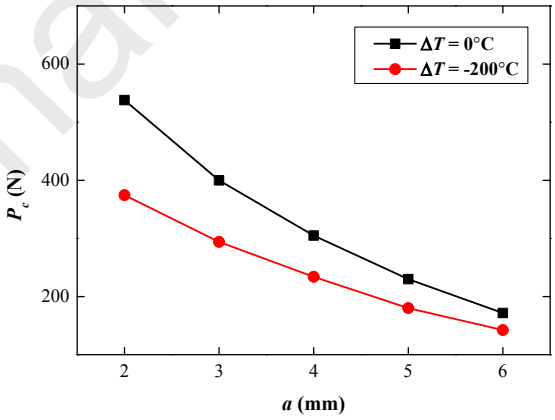


**Fig. 24.** Critical applied loads of the FPB specimens with varying values of pre-crack length under loading conditions with or without thermal effects.

Typically, the critical applied loads $P_c$ of FPS tests for different values of pre-crack length $a$ are shown in Fig. 24. As presented in Fig. 24, the critical applied load decreases rapidly with increasing of pre-crack length $a$. When the residual thermal effect is considered, the critical applied loads are much smaller than these tests without temperature variation. Which shows

that the residual thermal effect has a significantly negative effect on the bonded joints strength.

**Table 5. Material properties of two beams**

| Material | Elastic modulus $E$ (GPa) | Poisson's ratio $\nu$ | Density $\rho$ (kg/m$^3$) | Thermal exp. coeff. $\beta$ ($10^{-6}$/°C) |
|---|---|---|---|---|
| S45C | 206 | 0.30 | 3120 | 11.71 |
| $Si_3N_4$ | 289 | 0.25 | 7850 | 4.2 |

## 6. Conclusions

In this study, the peridynamics-based models are proposed for the fracture analysis of dissimilar material interface with the residual thermal effects. First, the peridynamic thermomechanical elastic model is presented. An extended peridynamic mixed-mode bond failure model is introduced for interface fracture analysis, and the peridynamic contact model is presented for frictional contact modeling. Then, three examples of the single edge-notched bimaterial (SENB), asymmetric bimaterial cantilever beams (ABCB) and four-point shearing (FPS) tests, are analyzed for the model verification and application.

In these numerical tests, the present peridynamic models can well capture the elastic and fracture behaviors of specimens. The deformations due to residual thermal effect and crack surface contact are modeled with the peridynamic thermomechanical and contact models. The energy release rates and mode mixity of SENB and ABCB specimens are computed and compared to the FEM solutions, and the interface fracture behaviors are predicted with the mixed-mode peridynamic failure model. And the results show that the residual thermal has a significantly effect on fracture behaviors of the material interface, it can largely increase the values of total energy release rate and the mode mixity of interface cracks, and decrease the strength of the bonded joints.

In summary, the whole framework of the peridynamic thermo-mechanical models for the material interface elastic and fracture analysis is established, with which the residual thermal effect on the interfacial facture can be well investigated. And it can be further applied for quantitatively fracture analysis of composite materials and bonded joints with the thermomechanical consideration.

**Acknowledgements**

The financial supports from the National Natural Science Foundation of China (Nos. 12172192, 12102226) and the China Postdoctoral Science Foundation (No. 2021M691798) are gratefully acknowledged.

**References**

[1] J.R. Rice, G.C. Sih, Plane problems of cracks in dissimilar media, J. Appl. Mech. 32 (1965) 418–423.

[2] J.W. Hutchinson, Z.G. Suo, Mixed mode cracking in layered materials, Adv. Appl. Mech. 29 (1992) 63–191.

[3] S.J. Howard, Y.C. Tsui, T.W. Clyne, The effect of residual stresses on the debonding of coatings-I. A model for delamination at a bimaterial interface, Acta Metall. Mater. 42 (1994) 2823–2836.

[4] M.E. Thurston, A.T. Zehnder, Nickel-alumina interfacial fracture toughness: experiments and analysis of residual stress effects, Int. J. Fract. 76 (1995) 221–241.

[5] X. Xu, T. Zhu, Y. Li, Y. Dai, M. Nath, Y. Ye, N. Hu, Y. Li, X. Wang, Effect of particle grading on fracture behavior and thermal shock resistance of MgO-C refractories, J. Eur. Ceram. Soc. 42 (2022) 672–681.

[6] K. Fang, M. Fall, Insight into the mode I and mode II fracture toughness of the cemented backfill-rock interface: Effect of time, temperature and sulphate, Constr. Build. Mater. 262 (2020) 120860.

[7] R.L. Williamson, B.H. Rabin, J.T. Drake, Finite element analysis of thermal residual stresses at graded ceramic-metal interfaces. Part I. Model description and geometrical effects, J. Appl. Phys. 74 (1993) 1310–1320.

[8] G. Delette, J. Laurencin, S. Murer, D. Leguillon, Effect of residual stresses on the propagation of interface cracks between dissimilar brittle materials: Contribution of two and three-dimensional analyses, Eur. J. Mech. A/Solids. 35 (2012) 97–110.

[9] T. Ikeda, C.T. Sun, Stress intensity factor analysis for an interface crack between dissimilar isotropic materials under thermal stress, Int. J. Fract. 111 (2001) 229–249.

[10] V.N. Burlayenko, H. Altenbach, T. Sadowski, S.D. Dimitrova, Computational

simulations of thermal shock cracking by the virtual crack closure technique in a functionally graded plate, Comput. Mater. Sci. 116 (2016) 11–21.

[11] T. Belytschko, T. Black, Elastic crack growth in finite elements with minimal remeshing, Int. J. Numer. Methods Eng. 45 (1999) 601–620.

[12] S. Jiang, Y. Gu, C.-M. Fan, W. Qu, Fracture mechanics analysis of bimaterial interface cracks using the generalized finite difference method, Theor. Appl. Fract. Mech. 113 (2021) 102942.

[13] S. Chadaram, S.K. Yadav, Three-dimensional thermal fracture analysis of piezoelectric material by extended finite element methods, Eng. Fract. Mech. 256 (2021) 107981.

[14] S. Dölling, S. Bremm, A. Kohlstetter, J. Felger, W. Becker, Predicting thermally induced edge-crack initiation using finite fracture mechanics, Eng. Fract. Mech. 252 (2021) 107808.

[15] Q.Q. Zhou, L. Yang, C. Luo, F.W. Chen, Y.C. Zhou, Y.G. Wei, Thermal barrier coatings failure mechanism during the interfacial oxidation process under the interaction between interface by cohesive zone model and brittle fracture by phase-field, Int. J. Solids Struct. 214–215 (2021) 18–34.

[16] W. Yang, A. Pourasghar, Z. Chen, Nonlocal fracture analysis of an interface crack between a functionally graded coating and a homogeneous substrate under thermal loading, Compos. Struct. 257 (2021) 113096.

[17] S.A. Silling, Reformulation of elasticity theory for discontinuities and long-range forces, J. Mech. Phys. Solids. 48 (2000) 175–209.

[18] S.A. Silling, M. Epton, O. Weckner, J. Xu, E. Askari, Peridynamic states and constitutive modeling, J. Elast. 88 (2007) 151–184.

[19] H. Zhang, P. Qiao, A two-dimensional ordinary state-based peridynamic model for elastic and fracture analysis, Eng. Fract. Mech. 232 (2020) 107040.

[20] X. Gu, E. Madenci, Q. Zhang, Revisit of non-ordinary state-based peridynamics, Eng. Fract. Mech. 190 (2018) 31–52.

[21] T.L. Warren, S.A. Silling, A. Askari, O. Weckner, M.A. Epton, J. Xu, A non-ordinary state-based peridynamic method to model solid material deformation and fracture, Int. J. Solids Struct. 46 (2009) 1186–1195.

[22] E. Madenci, S. Oterkus, Ordinary state-based peridynamics for plastic deformation according to von Mises yield criteria with isotropic hardening, J. Mech. Phys. Solids. 86 (2016) 192–219.

[23] C.T. Nguyen, S. Oterkus, Ordinary state-based peridynamic model for geometrically nonlinear analysis, Eng. Fract. Mech. 224 (2020) 106750.

[24] V. Diana, S. Casolo, A full orthotropic micropolar peridynamic formulation for linearly elastic solids, Int. J. Mech. Sci. 160 (2019) 140–155.

[25] V. Diana, R. Ballarini, Crack kinking in isotropic and orthotropic micropolar peridynamic solids, Int. J. Solids Struct. 196–197 (2020) 76–98.

[26] H. Pashazad, M. Kharazi, A peridynamic plastic model based on von Mises criteria with isotropic, kinematic and mixed hardenings under cyclic loading, Int. J. Mech. Sci. 156 (2019) 182–204.

[27] J. O'Grady, J. Foster, Peridynamic plates and flat shells: A non-ordinary, state-based model, Int. J. Solids Struct. 51 (2014) 4572–4579.

[28] J. O'Grady, J. Foster, Peridynamic beams: A non-ordinary, state-based model, Int. J. Solids Struct. 51 (2014) 3177–3183.

[29] S.R. Chowdhury, P. Roy, D. Roy, J.N. Reddy, A peridynamic theory for linear elastic shells, Int. J. Solids Struct. 84 (2016) 110–132.

[30] C. Diyaroglu, E. Oterkus, S. Oterkus, E. Madenci, Peridynamics for bending of beams and plates with transverse shear deformation, Int. J. Solids Struct. 69–70 (2015) 152–168.

[31] S.A. Silling, E. Askari, A meshfree method based on the peridynamic model of solid mechanics, Comput. Struct. 83 (2005) 1526–1535.

[32] H. Zhang, P. Qiao, A state-based peridynamic model for quantitative fracture analysis, Int. J. Fract. 211 (2018) 217–235.

[33] J.T. Foster, S.A. Silling, W. Chen, An energy based failure criterion for use with peridynamic states, Int. J. Multiscale Comput. Eng. 9 (2011) 675–687.

[34] Y. Zhang, P. Qiao, A new bond failure criterion for ordinary state-based peridynamic mode II fracture analysis, Int. J. Fract. 215 (2019) 105–128.

[35] H. Zhang, X. Zhang, P. Qiao, A new peridynamic mixed-mode bond failure model for

interface delamination and homogeneous materials fracture analysis, Comput. Methods Appl. Mech. Eng. 379 (2021) 113728.

[36] Y. Wang, F. Han, G. Lubineau, Strength-induced peridynamic modeling and simulation of fractures in brittle materials, Comput. Methods Appl. Mech. Eng. 374 (2021) 113558.

[37] H. Zhang, P. Qiao, L. Lu, Failure analysis of plates with singular and non-singular stress raisers by a coupled peridynamic model, Int. J. Mech. Sci. 157–158 (2019) 446–456.

[38] H. Zhang, P. Qiao, A coupled peridynamic strength and fracture criterion for open-hole failure analysis of plates under tensile load, Eng. Fract. Mech. 204 (2018) 103–118.

[39] W. Hu, Y.D. Ha, F. Bobaru, S.A. Silling, The formulation and computation of the nonlocal J-integral in bond-based peridynamics, Int. J. Fract. 176 (2012) 195–206.

[40] C. Stenström, K. Eriksson, The J-contour integral in peridynamics via displacements, Int. J. Fract. 216 (2019) 173–183.

[41] H. Zhang, P. Qiao, On the computation of energy release rates by a peridynamic virtual crack extension method, Comput. Methods Appl. Mech. Eng. 363 (2020) 112883.

[42] H. Zhang, P. Qiao, Virtual crack closure technique in peridynamic theory, Comput. Methods Appl. Mech. Eng. 372 (2020) 113318.

[43] D. Yang, X. He, J. Zhu, Z. Bie, A novel damage model in the peridynamics-based cohesive zone method (PD-CZM) for mixed mode fracture with its implicit implementation, Comput. Methods Appl. Mech. Eng. 377 (2021) 113721.

[44] D. Yang, X. He, X. Liu, Y. Deng, X. Huang, A peridynamics-based cohesive zone model (PD-CZM) for predicting cohesive crack propagation, Int. J. Mech. Sci. 184 (2020) 105830.

[45] Y. Tong, W. Shen, J. Shao, J. Chen, A new bond model in peridynamics theory for progressive failure in cohesive brittle materials, Eng. Fract. Mech. 223 (2020) 106767.

[46] P. Roy, A. Pathrikar, S.P. Deepu, D. Roy, Peridynamics damage model through phase field theory, Int. J. Mech. Sci. 128–129 (2017) 181–193.

[47] P. Diehl, S. Prudhomme, M. Lévesque, A Review of Benchmark Experiments for the Validation of Peridynamics Models, J. Peridynamics Nonlocal Model. 1 (2019) 14–35.

[48] K. Zhang, T. Ni, G. Sarego, M. Zaccariotto, Q. Zhu, U. Galvanetto, Experimental and numerical fracture analysis of the plain and polyvinyl alcohol fiber-reinforced ultra-

high-performance concrete structures, Theor. Appl. Fract. Mech. 108 (2020) 102566.

[49] D. Huang, G. Lu, C. Wang, P. Qiao, An extended peridynamic approach for deformation and fracture analysis, Eng. Fract. Mech. 141 (2015) 196–211.

[50] S. Niazi, Z. Chen, F. Bobaru, Crack nucleation in brittle and quasi-brittle materials: A peridynamic analysis, Theor. Appl. Fract. Mech. 112 (2021) 102855.

[51] Y.D. Ha, F. Bobaru, Characteristics of dynamic brittle fracture captured with peridynamics, Eng. Fract. Mech. 78 (2011) 1156–1168.

[52] M.J. Dai, S. Tanaka, S. Oterkus, E. Oterkus, Mixed-mode stress intensity factors evaluation of flat shells under in-plane loading employing ordinary state-based peridynamics, Theor. Appl. Fract. Mech. 112 (2021) 102841.

[53] D. Yang, W. Dong, X. Liu, S. Yi, X. He, Investigation on mode-I crack propagation in concrete using bond-based peridynamics with a new damage model, Eng. Fract. Mech. 199 (2018) 567–581.

[54] D. Yang, X. He, S. Yi, Y. Deng, X. Liu, Coupling of peridynamics with finite elements for brittle crack propagation problems, Theor. Appl. Fract. Mech. 107 (2020) 102505.

[55] B. Kilic, E. Madenci, Prediction of crack paths in a quenched glass plate by using peridynamic theory, Int. J. Fract. 156 (2009) 165–177.

[56] B. Kilic, E. Madenci, Peridynamic theory for thermomechanical analysis, IEEE Trans. Adv. Packag. 33 (2010) 97–105.

[57] H. Zhang, P. Qiao, An extended state-based peridynamic model for damage growth prediction of bimaterial structures under thermomechanical loading, Eng. Fract. Mech. 189 (2018) 81–97.

[58] C. Tien, S. Oterkus, Peridynamics for the thermomechanical behavior of shell structures, Eng. Fract. Mech. 219 (2019) 106623.

[59] Z. Yang, Y. Zhang, P. Qiao, An axisymmetric ordinary state-based peridynamic model for thermal cracking of linear elastic solids, Theor. Appl. Fract. Mech. 112 (2021) 102888.

[60] F. Bobaru, M. Duangpanya, The peridynamic formulation for transient heat conduction, Int. J. Heat Mass Transf. 53 (2010) 4047–4059.

[61] F. Bobaru, M. Duangpanya, A peridynamic formulation for transient heat conduction in

bodies with evolving discontinuities, J. Comput. Phys. 231 (2012) 2764–2785.

[62] Y. Wang, X. Zhou, M. Kou, A coupled thermo-mechanical bond-based peridynamics for simulating thermal cracking in rocks, Int. J. Fract. 211 (2018) 13–42.

[63] S. Oterkus, E. Madenci, A. Agwai, Fully coupled peridynamic thermomechanics, J. Mech. Phys. Solids. 64 (2014) 1–23.

[64] Y. Gao, S. Oterkus, Ordinary state-based peridynamic modelling for fully coupled thermoelastic problems, Contin. Mech. Thermodyn. 31 (2019) 907–937.

[65] Y. Gao, S. Oterkus, Fully coupled thermomechanical analysis of laminated composites by using ordinary state based peridynamic theory, Compos. Struct. 207 (2019) 397–424.

[66] W. Chen, X. Gu, Q. Zhang, X. Xia, A refined thermo-mechanical fully coupled peridynamics with application to concrete cracking, Eng. Fract. Mech. 242 (2021) 107463.

[67] Z. Yang, S.Q. Yang, M. Chen, Peridynamic simulation on fracture mechanical behavior of granite containing a single fissure after thermal cycling treatment, Comput. Geotech. 120 (2020) 103414.

[68] P. Seleson, M. Gunzburger, M.L. Parks, Interface problems in nonlocal diffusion and sharp transitions between local and nonlocal domains, Comput. Methods Appl. Mech. Eng. 266 (2013) 185–204.

[69] B. Alali, M. Gunzburger, Peridynamics and Material Interfaces, J. Elast. 120 (2015) 225–248.

[70] H. Zhang, X. Zhang, Y. Liu, P. Qiao, Peridynamic modeling of elastic bimaterial interface fracture, Comput. Methods Appl. Mech. Eng. 390 (2022) 114458.

[71] H. Ishikawa, A finite element analysis of stress intensity factors for combined tensile and shear loading by only a virtual crack extension, Int. J. Fract. 16 (1980) 243–246.

[72] A. Agrawal, A.M. Karlsson, Obtaining mode mixity for a bimaterial interface crack using the virtual crack closure technique, Int. J. Fract. 141 (2006) 75–98.

[73] F. Bobaru, M. Yang, L.F. Alves, S.A. Silling, E. Askari, J. Xu, Convergence, adaptive refinement, and scaling in 1D peridynamics, Int. J. Numer. Methods Eng. 77 (2009) 852–877.

[74] B. Kilic, E. Madenci, An adaptive dynamic relaxation method for quasi-static

simulations using the peridynamic theory, Theor. Appl. Fract. Mech. 53 (2010) 194–204.

Author statement:

Heng ZHANG (First Author): Conceptualization, Methodology, Software, Investigation, Formal Analysis, Writing - Original Draft;

Xiong ZHANG (Corresponding Author): Funding Acquisition, Resources, Supervision, Writing - Review & Editing.

Declaration of Interest Statement:

We declare that we have no known competing financial interests or personal relationships that could have appeared to influence the work entitled “Peridynamic analysis of materials interface fracture with thermal effect”.

# Peridynamic analysis of materials interface fracture with thermal effect[2]

**Heng Zhang[*], Xiong Zhang[**]**

[a] *School of Aerospace Engineering, Tsinghua University, Beijing 100084, China*

**Highlights:**

- A new thermomechanical peridynamic frame is established for the fracture analysis of dissimilar material interface coupled with residual thermal effect.
- An extended peridynamic mixed-mode failure model considering thermal effect is proposed for interfacial fracture predictions.
- A new peridynamic contact model is proposed for frictional contact modeling of crack surfaces.
- The proposed peridynamic models can successfully capture the role of residual thermal effect on the interfacial fracture.

[*] Email: hengzh@tsinghua.edu.cn

[**] Corresponding author. Email: xzhang@tsinghua.edu.cn